



Homogenization-based constitutive models for porous elastomers and implications for macroscopic instabilities: II—Results

O. Lopez-Pamies^{a,b}, P. Ponte Castañeda^{a,b,*}

^a*Department of Mechanical Engineering and Applied Mechanics, University of Pennsylvania, Philadelphia, PA 19104-6315, USA*

^b*LMS (CNRS UMR 7649), Département de Mécanique, École Polytechnique, 91128 Palaiseau, France*

Received 9 October 2006; received in revised form 13 January 2007; accepted 18 January 2007

Abstract

In Part I of this paper, we developed a homogenization-based constitutive model for the effective behavior of isotropic porous elastomers subjected to finite deformations. In this part, we make use of the proposed model to predict the overall response of porous elastomers with (compressible and incompressible) Gent matrix phases under a wide variety of loading conditions and initial values of porosity. The results indicate that the evolution of the underlying microstructure—which results from the finite changes in geometry that are induced by the applied loading—has a significant effect on the overall behavior of porous elastomers. Further, the model is in very good agreement with the exact and numerical results available from the literature for special loading conditions and generally improves on existing models for more general conditions. More specifically, we find that, in spite of the fact that Gent elastomers are strongly elliptic materials, the constitutive models for the porous elastomers are found to lose strong ellipticity at sufficiently large *compressive* deformations, corresponding to the possible onset of “macroscopic” (*shear* band-type) instabilities. This capability of the proposed model appears to be unique among theoretical models to date and is in agreement with numerical simulations and physical experience. The resulting elliptic and non-elliptic domains,

*Corresponding author. Department of Mechanical Engineering and Applied Mechanics, University of Pennsylvania, Philadelphia, PA 19104-6315, USA.

E-mail addresses: olp@seas.upenn.edu (O. Lopez-Pamies), ponte@seas.upenn.edu (P. Ponte Castañeda).

which serve to define the macroscopic “failure surfaces” of these materials, are presented and discussed in both strain and stress space.

© 2007 Elsevier Ltd. All rights reserved.

Keywords: Constitutive behavior; Finite strain; Microstructures; Porous material; Soft matter

1. Introduction

In the preceding paper (Lopez-Pamies and Ponte Castañeda, 2007), henceforth referred to as Part I, we developed—by means of the second-order homogenization method (Lopez-Pamies and Ponte Castañeda, 2006a)—a constitutive model for the mechanical response of porous elastomers subjected to finite deformations. More specifically, the type of porous elastomers under consideration were made up of initially spherical, polydisperse, vacuous inclusions distributed randomly and isotropically—in the undeformed configuration—in a compressible, and incompressible, isotropic elastomeric matrix.

The principal objective of the present work is to make use of the constitutive model proposed in Part I to generate a comprehensive understanding of the stress–strain behavior, the evolution of the underlying microstructure, and the onset of macroscopic instabilities—as determined by loss of strong ellipticity—in the class of porous elastomers under consideration here. Of particular interest is to provide insight concerning the subtle interplay between the evolution of the microstructure and the stability of these materials.

In the next section, we introduce the specific constitutive relations that will be used throughout this paper to characterize the matrix phase of the porous elastomers of interest. Moreover, we summarize briefly the results developed in Part I. For comparison purposes, we also recall earlier estimates for the effective behavior of porous elastomers. Section 3 deals with the presentation and discussion of the model predictions for a wide range of loading conditions, initial values of porosity, and matrix constitutive behavior, including macroscopic “failure surfaces” (Triantafyllidis and Bardenhagen, 1996) in strain and stress space. Finally, some general remarks will be drawn in Section 4.

2. Overall behavior of isotropic porous elastomers with Gent matrix

In Part I, we derived estimates for the effective stored-energy function \widehat{W} of porous elastomers consisting of a random and isotropic distribution of initially spherical, polydisperse voids in a general class of isotropic elastomeric matrix phases characterized by stored-energy functions of the form

$$W(\mathbf{F}) = \Phi(\lambda_1, \lambda_2, \lambda_3) = g(I) + h(J) + \frac{\kappa}{2}(J - 1)^2. \quad (1)$$

Here, $I = \mathbf{F} \cdot \mathbf{F} = \lambda_1^2 + \lambda_2^2 + \lambda_3^2$ and $J = \det \mathbf{F} = \lambda_1 \lambda_2 \lambda_3$ stand for, respectively, the first and third invariants associated with the deformation gradient tensor \mathbf{F} , with λ_i ($i = 1, 2, 3$) denoting the corresponding principal stretches. Moreover, g and h are material functions of their arguments, and the parameter κ denotes the bulk modulus of the material at zero strain. In this work, for definiteness, we will make use of a relatively simple model of the general form (1), capturing the limiting chain extensibility of elastomers, known as the

Gent (1996) model:

$$W(\mathbf{F}) = -\frac{J_m \mu}{2} \ln \left[1 - \frac{I-3}{J_m} \right] - \mu \ln J + \left(\frac{\kappa}{2} - \frac{J_m + 3}{3J_m} \mu \right) (J-1)^2. \quad (2)$$

In this expression, μ denotes the shear modulus of the material at zero strain and the parameter J_m indicates the limiting value for $I-3$ at which the elastomer locks up. Note that the stored-energy function (2) is strongly elliptic for all deformations provided that $\mu > 0$, $J_m > 0$, and $\kappa > 2\mu/J_m + 2/3\mu$, which will be assumed here. Note further that upon taking the limit $J_m \rightarrow \infty$ in (2), the Gent material reduces to the compressible Neo-Hookean solid:

$$W(\mathbf{F}) = \frac{\mu}{2} (I-3) - \mu \ln J + \left(\frac{\kappa}{2} - \frac{\mu}{3} \right) (J-1)^2. \quad (3)$$

Moreover, in order to recover incompressible behavior in (2), it suffices to take the limit $\kappa \rightarrow \infty$, in which case (2) reduces to

$$W(\mathbf{F}) = -\frac{J_m \mu}{2} \ln \left[1 - \frac{I-3}{J_m} \right], \quad (4)$$

together with the incompressibility constraint $J = 1$.

Having specified the constitutive behavior for the elastomeric matrix phase, we next spell out the specialization of the second-order estimates (SOEs) developed in Part I to porous elastomers with—the compressible and incompressible—Gent matrix phases characterized by the stored-energy functions (2) and (4). Before proceeding with the SOEs, however, it proves useful, for comparison purposes, to recall earlier estimates for the effective behavior of porous elastomers.

2.1. Earlier estimates

2.1.1. Voigt bound

As pointed out in Part I, there are very few homogenization-based estimates for the effective behavior of porous elastomers subjected to finite deformations. The most basic one is the Voigt upper bound due to Ogden (1978). When specialized to porous elastomers with initial porosity f_0 and Gent matrix phases of the form (2), this bound leads to

$$\widehat{W}(\overline{\mathbf{F}}) = \widehat{\Phi}(\overline{\lambda}_1, \overline{\lambda}_2, \overline{\lambda}_3) = (f_0 - 1) \left[\frac{J_m \mu}{2} \ln \left[1 - \frac{\overline{I} - 3}{J_m} \right] + \mu \ln \overline{J} - \left(\frac{\kappa}{2} - \frac{J_m + 3}{3J_m} \mu \right) (\overline{J} - 1)^2 \right], \quad (5)$$

where $\overline{I} = \overline{\mathbf{F}} \cdot \overline{\mathbf{F}} = \overline{\lambda}_1^2 + \overline{\lambda}_2^2 + \overline{\lambda}_3^2$ and $\overline{J} = \det \overline{\mathbf{F}} = \overline{\lambda}_1 \overline{\lambda}_2 \overline{\lambda}_3$ stand for, respectively, the first and third invariants associated with the macroscopic deformation gradient tensor $\overline{\mathbf{F}}$, and $\overline{\lambda}_i$ ($i = 1, 2, 3$) denote the corresponding principal stretches. The rigorous upper bound (5) depends only on the initial value of the porosity, f_0 , and contains no dependence on higher-order statistical information about the initial microstructure. Moreover, in the limit when the elastomeric matrix phase becomes incompressible (i.e., for $\kappa \rightarrow \infty$), expression (5) can be seen to become infinite for all deformations, except for isochoric loading paths (i.e., for loading paths with $\overline{J} = 1$), for which it reduces to

$$\widehat{W}^I(\overline{\mathbf{F}}) = \widehat{\Phi}^I(\overline{\lambda}_1, \overline{\lambda}_2, \overline{\lambda}_3) = (f_0 - 1) \frac{J_m \mu}{2} \ln \left[1 - \frac{\overline{I} - 3}{J_m} \right]. \quad (6)$$

In other words, the Voigt bound suggests that a porous elastomer with incompressible matrix phase is itself incompressible, which is in contradiction with experimental evidence. Finally, it is interesting to remark that—also in disagreement with physical evidence—the Voigt bounds (5) and (6) remain strongly elliptic for all deformations, provided that $\mu > 0$, $J_m > 0$, and $\kappa > 2\mu/J_m + 2/3\mu$, which has been assumed here.

2.1.2. Hashin estimate

In addition, an *exact* result has been given by Hashin (1985) for *hydrostatic loading* ($\bar{\lambda}_1 = \bar{\lambda}_2 = \bar{\lambda}_3 = \bar{\lambda}$) of porous elastomers with *incompressible*, isotropic matrix phase and the *Composite Sphere Assemblage* (CSA) microstructure (Hashin, 1962). When specialized to porous elastomers with incompressible Gent matrix phases of the form (4), the result reads as follows:

$$\widehat{W}^I(\bar{\mathbf{F}}) = \widehat{\Phi}^I(\bar{\lambda}, \bar{\lambda}, \bar{\lambda}) = -\frac{3J_m\mu}{2} \int_{f_0^{1/3}}^1 \ln \left[1 - \frac{I-3}{J_m} \right] R^2 dR, \tag{7}$$

where $I = 2\lambda^2 + \lambda^{-4}$ with $\lambda = (1 + (\bar{\lambda}^3 - 1)/R^3)^{1/3}$. The integral (7) can be computed analytically, but the final expression is too cumbersome to be included here. Instead, for illustrative purposes, we include the specialization of (7) to the simpler, limiting case of Neo-Hookean matrix phase (i.e., $J_m \rightarrow \infty$):

$$\widehat{W}^I(\bar{\mathbf{F}}) = \frac{3\mu}{2} (f_0 - 1 - \bar{\lambda}^{-1} + 2\bar{\lambda}^2 + f_0^{4/3}(\bar{\lambda}^3 + f_0 - 1))^{-1/3} - 2f_0^{1/3}(\bar{\lambda}^3 + f_0 - 1)^{2/3}. \tag{8}$$

2.1.3. The Danielsson–Parks–Boyce model

Finally, Danielsson et al. (2004)—making use of the work of Hou and Abeyaratne (1992)—have recently provided a model, henceforth referred to as the Danielsson–Parks–Boyce model (DPB) model, for isotropic porous elastomers with *incompressible*, isotropic matrix phases. When specialized to porous elastomers with incompressible Gent matrix phases of the form (4), the DPB estimate reads as follows:

$$\widehat{W}^I(\bar{\mathbf{F}}) = -\frac{3J_m\mu}{8\pi} \int_{f_0^{1/3}}^1 \int_0^{2\pi} \int_0^\pi \ln \left[1 - \frac{I-3}{J_m} \right] R^2 \sin \Theta d\Theta d\Psi dR. \tag{9}$$

In this expression,

$$I = \frac{1}{\bar{J}^{2/3}} \left[\bar{\psi}^2 \bar{T} + \frac{1}{R^2} (\bar{\lambda}_1^2 X_1^2 + \bar{\lambda}_2^2 X_2^2 + \bar{\lambda}_3^2 X_3^2) \left(\frac{1}{\bar{\psi}^4} - \bar{\psi}^2 \right) \right], \tag{10}$$

where \bar{T} and \bar{J} have already been defined above, $\bar{\psi} = (1 + (\bar{J} - 1)/R^3)^{1/3}$, and $X_1 = R \sin \Theta \sin \Psi$, $X_2 = R \sin \Theta \cos \Psi$, and $X_3 = R \cos \Theta$. In the limiting case of Neo-Hookean matrix phase (i.e., $J_m \rightarrow \infty$), it is possible to solve (9) in closed form. Following Danielsson et al. (2004) (Section 3.2), the corresponding final expression can be written as follows:

$$\widehat{W}^I(\bar{\mathbf{F}}) = \frac{\mu}{2} \left(2 - \frac{1}{\bar{J}} - \frac{f_0 + 2(\bar{J} - 1)}{\bar{J}^{2/3} \eta^{1/3}} \right) \bar{T} - \frac{3}{2} (1 - f_0) \mu, \tag{11}$$

where $\eta = 1 + (\bar{J} - 1)/f_0$.

At this point, it is important to remark that the DPB model is in fact a generalization of both the Voigt bound and the Hashin estimate, in the sense that it reduces to the Voigt bound for isochoric deformations and it recovers Hashin's exact solution for hydrostatic loading. This can be verified directly from relation (9). Indeed, it is easy to check that for $\bar{J} = \bar{\lambda}_1 \bar{\lambda}_2 \bar{\lambda}_3 = 1$, the DPB estimate (9) reduces to the Voigt bound (6) and for $\bar{\lambda}_1 = \bar{\lambda}_2 = \bar{\lambda}_3 = \bar{\lambda}$, to the Hashin estimate (7). For more general loadings, the DPB estimate can be shown to be actually a *rigorous upper bound* for porous elastomers with incompressible matrix phases and the *Composite Sphere Assemblage* (CSA) microstructure. The reasons for this result rely on the fact that the DPB model is constructed by making use of a *kinematically admissible* field in a spherical volume element (Danielsson et al., 2004). Then, by well known arguments (Hashin, 1962), it follows that the resulting estimate is an upper bound for porous elastomers with the CSA microstructure, much like the Gurson (1977) model is an upper bound for porous metals with ideally plastic matrix phase and the CSA microstructure. In conclusion, the DPB model is expected to be too “stiff”—given that it is an upper bound—for general loading conditions, with the exception of hydrostatic loading, for which it should be very accurate (in fact, it is exact for the CSA microstructure).

2.2. Second-order estimates

2.2.1. Compressible Gent matrix

Following Section 4.1 of Part I, the SOE for the effective stored-energy function \widehat{W} of a porous elastomer with initial porosity f_0 and *compressible*, elastomeric matrix phase characterized by the stored-energy function (2) is given by

$$\begin{aligned} \widehat{W}(\bar{\mathbf{F}}) &= \widehat{\Phi}(\bar{\lambda}_1, \bar{\lambda}_2, \bar{\lambda}_3) \\ &= (1 - f_0) \left[-\frac{J_m \mu}{2} \ln \left[1 - \frac{\hat{I}^{(1)} - 3}{J_m} \right] \right. \\ &\quad - \mu \ln \hat{J}^{(1)} + \left(\frac{\kappa}{2} - \frac{J_m + 3}{3J_m} \mu \right) (\hat{J}^{(1)} - 1)^2 \\ &\quad - (\hat{F}_{11}^{(1)} - \bar{\lambda}_1^{(1)}) (2\bar{g}_I \bar{\lambda}_1 + \bar{h}_J \bar{\lambda}_2 \bar{\lambda}_3 + \kappa(\bar{J} - 1) \bar{\lambda}_2 \bar{\lambda}_3) \\ &\quad - (\hat{F}_{22}^{(1)} - \bar{\lambda}_2^{(1)}) (2\bar{g}_I \bar{\lambda}_2 + \bar{h}_J \bar{\lambda}_1 \bar{\lambda}_3 + \kappa(\bar{J} - 1) \bar{\lambda}_1 \bar{\lambda}_3) \\ &\quad \left. - (\hat{F}_{33}^{(1)} - \bar{\lambda}_3^{(1)}) (2\bar{g}_I \bar{\lambda}_3 + \bar{h}_J \bar{\lambda}_1 \bar{\lambda}_2 + \kappa(\bar{J} - 1) \bar{\lambda}_1 \bar{\lambda}_2) \right], \end{aligned} \quad (12)$$

where $\bar{g}_I = J_m \mu / [2(J_m + 3 - \bar{I})]$, $\bar{h}_J = -\mu / J_m - 2\mu / (3J_m)(3 + J_m)(\bar{J} - 1)$ have been introduced for ease of notation, and it is recalled that $\bar{I} = \bar{\mathbf{F}} \cdot \bar{\mathbf{F}} = \bar{\lambda}_1^2 + \bar{\lambda}_2^2 + \bar{\lambda}_3^2$ and $\bar{J} = \det \bar{\mathbf{F}} = \bar{\lambda}_1 \bar{\lambda}_2 \bar{\lambda}_3 = 1$. In addition, the variables $\bar{\lambda}_1^{(1)}, \bar{\lambda}_2^{(1)}, \bar{\lambda}_3^{(1)}, \hat{F}_{11}^{(1)}, \hat{F}_{22}^{(1)}, \hat{F}_{33}^{(1)}, \hat{I}^{(1)}$, and $\hat{J}^{(1)}$ are obtained from expressions (41), (43), and (48) in Appendix B of Part I. They are functions of the applied loading, $\bar{\lambda}_1, \bar{\lambda}_2, \bar{\lambda}_3$, the initial porosity, f_0 , the matrix constitutive

parameters, μ , κ , J_m , as well as of the seven variables ℓ_α^* ($\alpha = 1, 2, \dots, 7$) that are the numerical solution of the non-linear system of algebraic equations (46) in Appendix B of Part I.

2.2.2. Incompressible Gent matrix

The corresponding effective stored-energy function \widehat{W}^I for a porous elastomer with *incompressible* elastomeric matrix phase characterized by the stored-energy function (4) is obtained by taking the limit of $\kappa \rightarrow \infty$ in (12), as discussed in Appendix C of Part I. The final result reads as follows:

$$\widehat{W}^I(\overline{\mathbf{F}}) = \widehat{\Phi}^I(\overline{\lambda}_1, \overline{\lambda}_2, \overline{\lambda}_3) = (f_0 - 1) \frac{J_m \mu}{2} \ln \left[1 - \frac{\hat{I}^{(1)} - 3}{J_m} \right]. \quad (13)$$

Here, the variable $\hat{I}^{(1)}$ is given by expression (62) in Appendix C of Part I, and depends ultimately on the applied loading, $\overline{\lambda}_1, \overline{\lambda}_2, \overline{\lambda}_3$, the initial porosity, f_0 , the matrix constitutive parameters, μ , J_m , as well as on the seven variables u_α ($\alpha = 1, 2, \dots, 7$) defined by (60) in Part I, which are the solution of the system of seven non-linear, algebraic equations formed by relations (57) and (58) in Part I (Appendix C). Except for certain special loading conditions (see Section 4.2 of Part I), these equations must be solved numerically.

3. Results and discussion

In this section, the constitutive models (12) and (13) are used to study the effective stress–strain response, the microstructure evolution, and the macroscopic stability of porous elastomers with Gent matrix phases under different types of finite deformations. Results are given for various values of the compressibility ratio κ/μ and lock-up parameter J_m , as well as various values of initial porosity f_0 and are computed up to the point at which either the associated effective incremental modulus is found to lose strong ellipticity (see Section 2 of Part I), or, alternatively, the porosity is found to vanish. If neither of these phenomena occurs, the results are truncated at some sufficiently large value of the deformation. For clarity, the points at which the homogenized material loses strong ellipticity are indicated with the symbol “ \circ ” in the figures, whereas the symbol “ \diamond ” is utilized to indicate the vanishing of the porosity.

The results presented in this section are organized as follows. First, we address the effective response of Gent porous elastomers subjected to *axisymmetric loading conditions*. Special attention is given to *hydrostatic*, *biaxial*, and *uniaxial* tension/compression loadings, which, beyond providing comprehensive physical insight and contributing to establish the accuracy of the proposed models through comparisons with the available exact results, happen to correspond to actual loading conditions easily achievable with standard experimental equipment. Following the axisymmetric subsection, we provide representative results for the overall behavior of Gent porous elastomers subjected to *plane-strain loading conditions*. In particular, we focus on *pure shear* and *in-plane uniaxial* tension/compression loadings. The corresponding macroscopic failure surfaces, as determined by the loss of strong ellipticity of the homogenized behavior of the material, are presented—in principal strain and stress spaces—and discussed for the axisymmetric, as well as for the plane-strain loading conditions.

3.1. Axisymmetric loadings

3.1.1. Hydrostatic tension/compression

Fig. 1 presents the comparison between the effective behavior as predicted by the SOE (13) and the “exact” (Hashin, 1985) estimate (8) for a porous elastomer with incompressible Neo-Hookean matrix phase under hydrostatic loading ($\bar{\lambda}_1 = \bar{\lambda}_2 = \bar{\lambda}_3 = \bar{\lambda}$). Recall that the DPB model (11) coincides identically with the exact result (8) in this case. Results are shown for initial porosities of 10%, 30%, and 50% as a function of the logarithmic strain $\bar{e} = \ln \bar{\lambda}$. Part (a) shows the normalized macroscopic stress $\bar{S}/\mu = \mu^{-1} \partial \bar{\Phi}^I / \partial \bar{\lambda}_1 = \mu^{-1} \partial \bar{\Phi}^I / \partial \bar{\lambda}_2 = \mu^{-1} \partial \bar{\Phi}^I / \partial \bar{\lambda}_3$, and part (b), the associated evolution of the porosity f . It is observed from Fig. 1(a) that the SOE predictions are in very good agreement with the exact result. Note that the agreement improves for higher values of initial porosity f_0 . It is also discerned from Fig. 1(a) that the effective behavior of the material is softer for higher values of f_0 , as expected on physical grounds. Interestingly, it is further recognized from Fig. 1(a) that the overall response of the porous elastomer under hydrostatic compression exhibits very significant stiffening, but that, under hydrostatic tension, the behavior gets more compliant with increasing strain. In this connection, we note from Fig. 1(b) that the porosity decreases for compressive deformations and increases for tensile ones. This entails a *geometric* stiffening/softening mechanism that is entirely consistent with the stress–strain results shown in Fig. 1(a). With regard to the remaining microstructural variables, it should be realized that they do not evolve under hydrostatic loading, that is, the initially spherical shape and distribution of the underlying pores remain—on average—spherical for all applied hydrostatic deformations. Turning back to Fig. 1(b), we remark that the predictions for the evolution of the porosity f as determined by the SOE are in very good agreement with the exact result

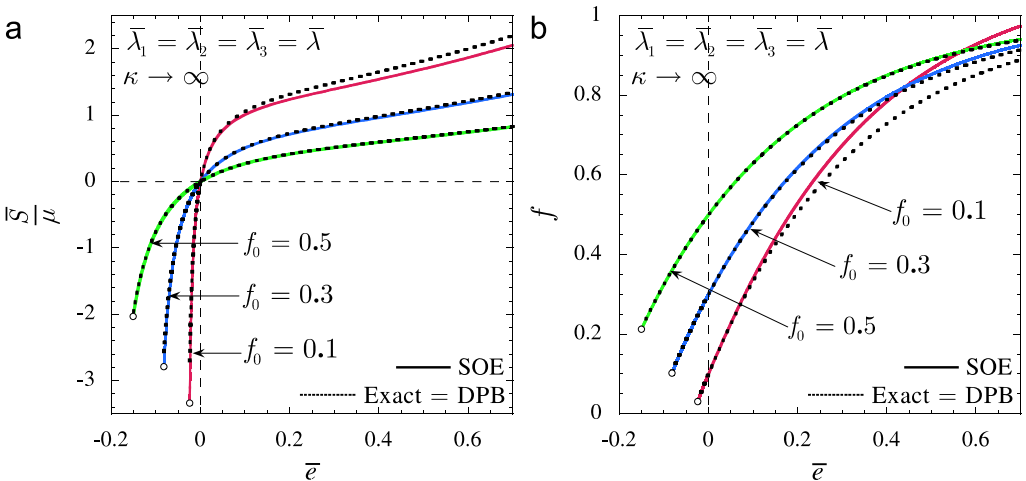


Fig. 1. Comparisons of the effective response, as predicted by the second-order estimate (SOE) (13), with the exact results (Hashin, 1985), of a porous elastomer with incompressible matrix phase subjected to hydrostatic tension and compression ($\bar{\lambda}_1 = \bar{\lambda}_2 = \bar{\lambda}_3 = \bar{\lambda}$). The results correspond to a material with Neo-Hookean matrix phase and various values of initial porosity f_0 and are shown as a function of the logarithmic strain $\bar{e} = \ln \bar{\lambda}$. (a) The normalized macroscopic stress $\bar{S}/\mu = \mu^{-1} \partial \bar{\Phi}^I / \partial \bar{\lambda}_1 = \mu^{-1} \partial \bar{\Phi}^I / \partial \bar{\lambda}_2 = \mu^{-1} \partial \bar{\Phi}^I / \partial \bar{\lambda}_3$. (b) The evolution of the porosity f .

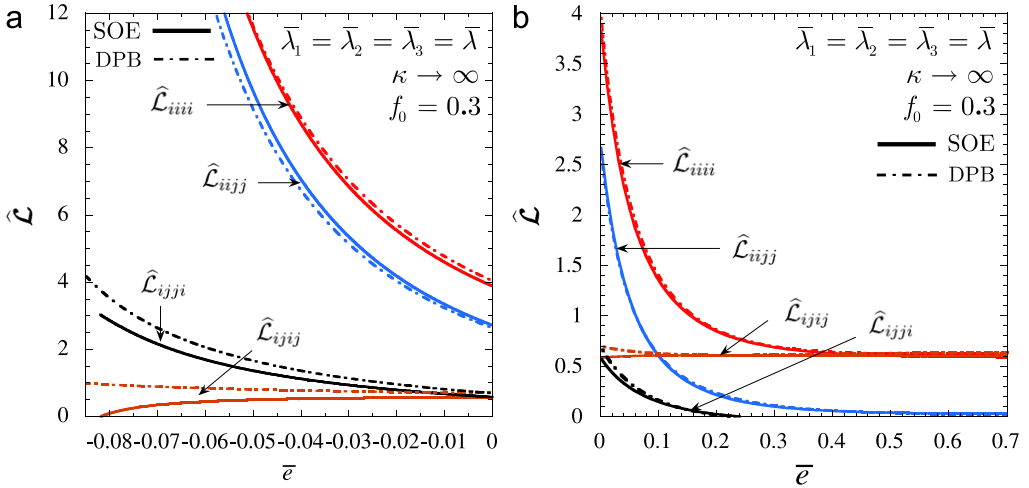


Fig. 2. Effective response, as predicted by the second-order estimate (SOE) (13) and the DPB model (11), of a porous elastomer with incompressible matrix phase subjected to hydrostatic loading ($\bar{\lambda}_1 = \bar{\lambda}_2 = \bar{\lambda}_3 = \bar{\lambda}$). The results correspond to a material with Neo-Hookean matrix phase and initial porosity of $f_0 = 30\%$ and are shown as a function of the logarithmic strain $\bar{\epsilon} = \ln \bar{\lambda}$. (a) The non-zero components ($i, j \in \{1, 2, 3\}$, $i \neq j$, no summation) of the effective incremental modulus $\widehat{\mathcal{L}}$ —written with respect to the Lagrangian principal axes—for hydrostatic compression ($\bar{\lambda} \leq 1$). (b) The corresponding results for hydrostatic tension ($\bar{\lambda} \geq 1$).

(see Eq. (31) in Part I) for the cases of 30% and 50% initial porosity. The agreement between the prediction and the exact result for the case of $f_0 = 10\%$ is excellent for hydrostatic compression, but it deteriorates appreciably for tensile hydrostatic deformations larger than $\bar{\epsilon} = \ln \bar{\lambda} = 0.2$. This has the effect of slightly exaggerating the geometric softening in tension for $f_0 = 10\%$, leading to slightly softer predictions than the Hashin estimate. Finally, it should be noticed from Fig. 1 that the homogenized response of the porous elastomer, as predicted by the SOE, becomes unstable—through loss of strong ellipticity—under hydrostatic compression (denoted by the symbol “o”), while it remains strongly elliptic under hydrostatic tension. This result is investigated in more detail in the context of the next two figures.

Fig. 2 provides results associated with those shown in Fig. 1 for the components¹ of the normalized effective incremental modulus $\widehat{\mathcal{L}} = \mu^{-1} \partial^2 \widehat{W}^I / \partial \mathbf{F}^2$ of a porous elastomer with incompressible, Neo-Hookean matrix phase and initial porosity of 30% under hydrostatic loading ($\bar{\lambda}_1 = \bar{\lambda}_2 = \bar{\lambda}_3 = \bar{\lambda}$). Part (a) shows results for hydrostatic compression ($\bar{\lambda} \leq 1$), and part (b), for hydrostatic tension ($\bar{\lambda} \geq 1$). Fig. 2(a) illustrates that—in accord with the stress–strain results shown in Fig. 1(a)—the normal components $\widehat{\mathcal{L}}_{1111}$, $\widehat{\mathcal{L}}_{2222}$, and $\widehat{\mathcal{L}}_{3333}$, as predicted by the SOE (13), increase rapidly with the applied compressive strain. That is, the porous elastomer *stiffens* very significantly in the “direction” of the applied loading. On the other hand, the effective incremental shear response of the porous elastomer, as measured² by $\widehat{\mathcal{L}}_{1212}$, $\widehat{\mathcal{L}}_{1313}$, and $\widehat{\mathcal{L}}_{2323}$, is seen to *soften* with the applied hydrostatic compression to the point that $\widehat{\mathcal{L}}_{1212} = \widehat{\mathcal{L}}_{1313} = \widehat{\mathcal{L}}_{2323} = 0$ at some critical finite stretch

¹Here and subsequently, the components of the effective incremental modulus $\widehat{\mathcal{L}}$ are referred to the macroscopic Lagrangian principal axes, i.e., the principal axes of $\mathbf{F}^T \mathbf{F}$.

²Recall that for isotropic materials $\widehat{\mathcal{L}}_{ijj} = \widehat{\mathcal{L}}_{jji}$ ($i, j \in \{1, 2, 3\}$, $i \neq j$, no summation).

$\bar{\lambda}_{\text{crit}}$. This critical stretch corresponds to the point at which the porous elastomer loses strong ellipticity. In this connection, it should be remarked that the combinations $\widehat{\mathcal{L}}_{iii}\widehat{\mathcal{L}}_{jjj} + \widehat{\mathcal{L}}_{ijj}^2 - (\widehat{\mathcal{L}}_{ijj} + \widehat{\mathcal{L}}_{iji})^2 + 2\widehat{\mathcal{L}}_{ijj}\sqrt{\widehat{\mathcal{L}}_{iii}\widehat{\mathcal{L}}_{jjj}}$ ($i, j \in \{1, 2, 3\}, i \neq j$, no summation) also vanish at $\bar{\lambda}_{\text{crit}}$. Thus, making contact with Appendix A of Part I, this means that conditions (33) and (34) in Part I cease to hold true. Physically, this implies that the porous elastomer may develop localized deformations in planar zones with arbitrary normals \mathbf{N} . Furthermore, the deformation in these zones localizes in shear, since $\mathbf{m} \perp \mathbf{N}$. (Recall from Section 2 of Part I that \mathbf{m} denotes the eigenvector corresponding to the zero eigenvalue of the acoustic tensor associated with \mathbf{N} , so that it characterizes the type of deformation within the localized band.) This remarkable behavior predicted by the SOE is consistent with numerical simulations (Michel et al., 2007), as well as with physical evidence (see, e.g., Kinney et al., 2001; Gong and Kyriakides, 2005). Indeed, local buckling of matrix ligaments is anticipated to occur in porous elastomers subjected to *compressive* states of deformation. In turn, connected networks of buckled ligaments that extend throughout the entire specimen correspond to bands of *localized deformation* at the macroscopic level. The development of these macroscopic bands of localized deformation may correspond to the loss of strong ellipticity of the homogenized behavior of the material (Geymonat et al., 1993). Comparing now the SOE with the DPB predictions in Fig. 2(a), it is observed that the normal components $\widehat{\mathcal{L}}_{1111}$, $\widehat{\mathcal{L}}_{2222}$, and $\widehat{\mathcal{L}}_{3333}$ of both models are in very good agreement. In contrast, the effective incremental shear moduli $\widehat{\mathcal{L}}_{1212}$, $\widehat{\mathcal{L}}_{1313}$, and $\widehat{\mathcal{L}}_{2323}$ predicted by the DPB model are much stiffer than the corresponding SOE results. In fact, they exhibit different trends: while the SOE shear moduli decrease with the applied loading, the DPB shear moduli increase, which ultimately entails that the DPB model remains strongly elliptic for all applied hydrostatic compression (in disagreement with numerical results and physical experience). Turning now to Fig. 2(b), it is noticed that—in accord with the stress–strain results shown in Fig. 1(a)—the normal components $\widehat{\mathcal{L}}_{1111}$, $\widehat{\mathcal{L}}_{2222}$, and $\widehat{\mathcal{L}}_{3333}$ decrease very distinctly with the applied hydrostatic tension. That is, the porous elastomer *softens* in the “direction” of loading with the applied tensile strain. Conversely, the effective incremental shear moduli $\widehat{\mathcal{L}}_{1212}$, $\widehat{\mathcal{L}}_{1313}$, and $\widehat{\mathcal{L}}_{2323}$ are seen to increase—though very slightly. Furthermore, Fig. 2(b) also shows more explicitly the fact (already mentioned above) that there is no loss of strong ellipticity for hydrostatic tension. Note that—as opposed to hydrostatic compression—the SOE and DPB predictions in Fig. 2(b) are in very good agreement for the normal as well as for the shear effective moduli. Note finally that the results shown in Fig. 2 for $f_0 = 0.3$ are representative for all values of initial porosity, since the trends followed by the components of $\widehat{\mathcal{L}}$ for all values of f_0 are similar to those displayed in Fig. 2. The precise effect of f_0 on the effective incremental behavior and stability of porous elastomers subjected to hydrostatic loading will be addressed in detail in the context of the next figure.

In short, Fig. 2 puts into evidence the subtle influence of the evolution of the underlying microstructure on the effective behavior and stability of porous elastomers subjected to finite deformations. Indeed, the *stiffening* of the effective incremental normal response of the porous elastomer—as measured by $\widehat{\mathcal{L}}_{1111}$, $\widehat{\mathcal{L}}_{2222}$, and $\widehat{\mathcal{L}}_{3333}$ —when subjected to hydrostatic compression (see Fig. 2(a)) is entirely consistent with the decrease of porosity illustrated in Fig. 1(b). However, as shown in Fig. 2(a), the decrease of porosity does also lead to the geometric *softening* of the effective incremental shear response of the

material—as measured by $\widehat{\mathcal{L}}_{1212}$, $\widehat{\mathcal{L}}_{1313}$, and $\widehat{\mathcal{L}}_{2323}$ —which eventually leads to the loss of strong ellipticity of the porous elastomer at some finite stretch (in spite of the fact that the elastomeric matrix phase is strongly elliptic). Analogously, the *softening* of the effective incremental normal response of the porous elastomer when subjected to hydrostatic tension (see Fig. 2(b)) is entirely consistent with the increase of porosity illustrated in Fig. 1(b). Further, the increase of porosity does also lead to the (slight) geometric *stiffening* of the effective incremental shear response of the material, which, in some sense, prevents the porous elastomer from losing stability.

Fig. 3 provides plots associated with the results shown in Figs. 1 and 2 for (a) the critical stretch, $\bar{\lambda}_{\text{crit}}$, and (b) the normalized critical stress, $\bar{S}_{\text{crit}}/\mu$, at which the SOE (13) loses strong ellipticity under hydrostatic compression as a function of the initial porosity f_0 . Fig. 3 exhibits two distinct regimes: the “dilute,” or small-porosity regime ($0 < f_0 < 0.1$), and the “finite,” or large-porosity regime ($0.1 < f_0 < 1$). Interestingly, for $0 < f_0 < 0.1$, Fig. 3 shows that the porous elastomer becomes more stable, in both, strain and stress space with increasing initial porosity. That is, in the small-porosity regime, the material loses strong ellipticity at smaller stretches $\bar{\lambda}_{\text{crit}}$ (larger compressive strains) and larger compressive stresses $\bar{S}_{\text{crit}}/\mu$, for higher values of the initial porosity f_0 . In passing, we remark that this rather counterintuitive result has already been observed in 2D porous elastomers with random and periodic microstructures (Lopez-Pamies and Ponte Castañeda, 2004; Michel et al., 2007). In contrast, for $0.1 < f_0 < 1$, the porous elastomer continues to improve its stability with increasing porosity in strain space; however, in stress space, the trend is reversed and the material is seen to become more unstable for higher values of f_0 . The fact that for the range of initial porosities $0.1 < f_0 < 1$ the critical stretch $\bar{\lambda}_{\text{crit}}$ exhibits a different trend than $\bar{S}_{\text{crit}}/\mu$ can be understood by recognizing that the stress–strain relation of the porous elastomer under hydrostatic compression softens drastically with increasing f_0 in this regime (see Fig. 1(a)). This implies that even though $|\bar{S}_{\text{crit}}/\mu|$ decreases with increasing

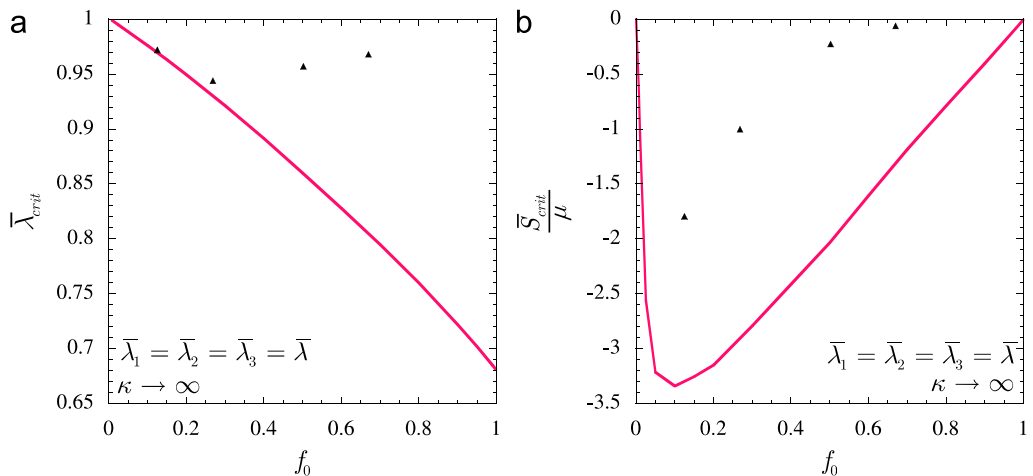


Fig. 3. Hydrostatic compression ($\bar{\lambda}_1 = \bar{\lambda}_2 = \bar{\lambda}_3 = \bar{\lambda} \leq 1$) of a porous elastomer with incompressible, Neo-Hookean matrix phase. (a) The critical stretch $\bar{\lambda}_{\text{crit}}$ at which the second-order estimate (13) loses strong ellipticity as a function of initial porosity f_0 . (b) The associated normalized critical stress $\bar{S}_{\text{crit}}/\mu$. The isolated data points in the plots correspond to experimental results for the critical buckling of spherical shells under hydrostatic compression (Wesolowski, 1967).

f_0 , the corresponding stretches $\bar{\lambda}_{\text{crit}}$ required to reach such critical stresses may, and in fact do, decrease with increasing f_0 . In connection with the results shown in Fig. 3, it is important to recall that, unlike for small and moderate values of porosity, the SOE predictions are not expected to be accurate—except for the CSA microstructure—for very large f_0 , as discussed in Section 3.1 of Part I. Whatever the case may be, it is interesting to note that, according to the SOE results, $\bar{S}_{\text{crit}}/\mu \rightarrow 0$ as $f_0 \rightarrow 1$, as it may be expected on physical grounds.

At this stage, it is important to remark that while the work of Hashin (1985) provides exact results for the effective stored-energy function, \widehat{W} , and the porosity evolution, f , for the hydrostatic loading of porous elastomers with incompressible, isotropic matrix phase and the *Composite Sphere Assemblage* (CSA) microstructure, it contains essentially no information about the macroscopically stability of these materials. This is simply due to the fact that the exact results of Hashin are given for a *fixed* loading path—namely, $\bar{\lambda}_1 = \bar{\lambda}_2 = \bar{\lambda}_3$ —and therefore, the corresponding effective incremental modulus $\widehat{\mathcal{L}}$, needed for detecting loss of strong ellipticity, cannot be computed. On the other hand, it is possible to compute the effective incremental modulus associated with the DPB model (11), which as already stated agrees with the Hashin estimate for hydrostatic loading, and check for loss of strong ellipticity. It turns out, however, that—unlike the SOE (13)—the DPB model (11) remains strongly elliptic for all hydrostatic deformations, in contradiction with physical experience. More precisely, under this type of loading conditions—as illustrated in Fig. 2—the effective incremental modulus $\widehat{\mathcal{L}}$ associated with the DPB model not only remains strongly elliptic, but also stiffens significantly with increasing strain. This overly stiff behavior seems to be consistent with the fact that the DPB model is a rigorous upper bound for CSA microstructures. Finally, it is fitting to mention that there have been a number of experimental and analytical studies (see, e.g., Wesolowski, 1967; Wang and Ertepinar, 1972) on the stability of isolated spherical shells under hydrostatic loading. Of course, the buckling instabilities of an isolated shell cannot be identified with the buckling instabilities that would take place in an actual porous elastomer with the CSA microstructure, except possibly in the dilute limit, when no interaction is expected among the pores. In this connection, we have included in Fig. 3 the experimental findings of Wesolowski (1967) comprising the critical stretches and pressures at which a Neo-Hookean, thick-walled, spherical shell first buckles as function of initial porosity (i.e., the cube of the ratio of inner to outer radius of the shell in the undeformed state). Remarkably, the experimental results of Wesolowski (1967) in strain space agree extremely well with the SOE predictions in the small-porosity regime, where the comparisons between the isolated shell and the porous elastomer may be relevant. For large values of initial porosity, it is interesting to observe that the SOE results provide a bound for the experimental “failure surface” characterized by the stretches and stresses at which the isolated shell first buckles.

3.1.2. Biaxial tension/compression

Fig. 4 presents the SOE predictions for the effective response of a porous elastomer with incompressible Gent matrix phase under biaxial loading ($\bar{\lambda}_2 = \bar{\lambda}_3 = \bar{\lambda}$, $\bar{S}_{11} = \partial \widehat{\Phi}^I / \partial \bar{\lambda}_1 = 0$). Results are shown for a matrix lock-up parameter of $J_m = 50$ and initial porosities of $f_0 = 0\%$, 10%, 30% and 50% as a function of the logarithmic strain $\bar{e} = \ln \bar{\lambda}$. Part (a) shows the normalized macroscopic “biaxial” stress $\bar{S}_{\text{bi}}/\mu = \bar{\mu}^{-1} \partial \widehat{\Phi}^I / \partial \bar{\lambda}_2 = \bar{\mu}^{-1} \partial \widehat{\Phi}^I / \partial \bar{\lambda}_3$, and part (b), the associated “lateral” strain $\bar{e}_{\text{lat}} = \ln \bar{\lambda}_1$. Similar to hydrostatic loading and as expected on physical grounds,

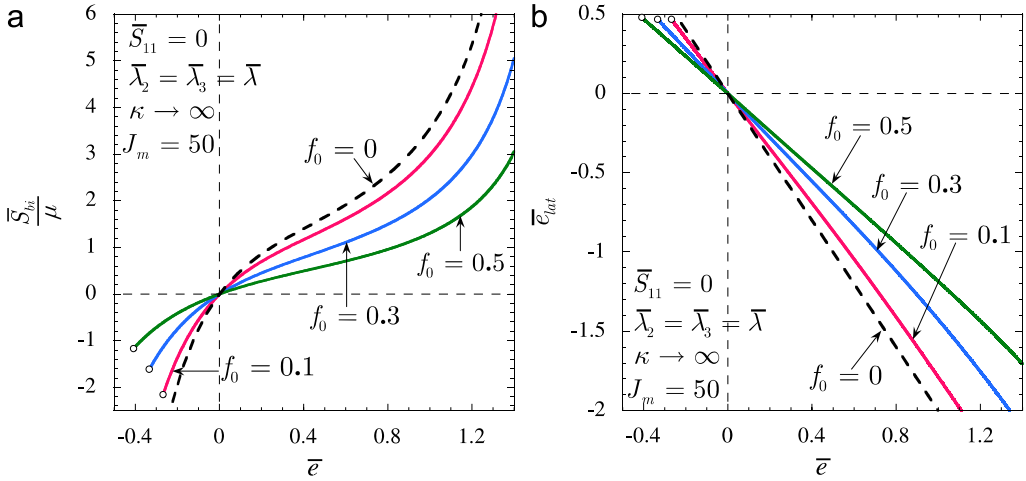


Fig. 4. Effective response, as predicted by the second-order estimate (13), of a porous rubber subjected to biaxial tension and compression ($\bar{\lambda}_2 = \bar{\lambda}_3 = \bar{\lambda}, \bar{S}_{11} = \partial \hat{\Phi}^I / \partial \bar{\lambda}_1 = 0$), as a function of the logarithmic strain $\bar{\epsilon} = \ln \bar{\lambda}$. The results correspond to a material with incompressible, Gent matrix with lock-up parameter $J_m = 50$ and various values of initial porosity f_0 . (a) The normalized macroscopic stress $\bar{S}_{bi}/\mu = \mu^{-1} \partial \hat{\Phi}^I / \partial \bar{\lambda}_2 = \mu^{-1} \partial \hat{\Phi}^I / \partial \bar{\lambda}_3$. (b) The lateral strain $\bar{\epsilon}_{lat} = \ln \bar{\lambda}_1$.

Fig. 4(a) shows that the effective response of the porous elastomer is softer for higher values of the initial porosity f_0 . Furthermore, for biaxial tension, as well as for compression, the material is seen to stiffen very significantly with increasing strain. In spite of this similarity, the porous elastomer is seen to become unstable—through loss of strong ellipticity—under biaxial compression, while it remains stable under biaxial tension. This disparity will be shown shortly to be due to differences in the evolution of the underlying microstructure. Turning now to Fig. 4(b), we notice that the volume of the porous elastomer increases (decreases) when subjected to biaxial tension (compression), that is, $\ln(\det \bar{\mathbf{F}}) = \bar{\epsilon}_{lat} + 2\bar{\epsilon} > (<) 0$. Since the elastomeric matrix phase is incompressible, this has the direct implication that the porosity increases (decreases) with the applied tensile (compressive) deformation. In this connection, it is interesting to remark further from Fig. 4(b) that for biaxial tension (compression) the porous elastomer undergoes a larger volume increase (decrease) for higher values of initial porosity f_0 .

Fig. 5 provides corresponding results for (a) the evolution of the porosity f and (b) the evolution of the average aspect ratios ω_1 and ω_2 (defined by Eq. (25) in Part I). Fig. 5(a) shows that the SOE predictions for the evolution of the porosity f virtually coincide with the “exact” result for all values of initial porosities considered. In this regard, we should make the following parenthetical clarification. As discussed in Section 4.4 of Part I, the evolution of porosity in porous elastomers with incompressible matrix phase can be computed exactly through expression (31) in Part I, provided that the determinant of the macroscopic deformation gradient, $\det \bar{\mathbf{F}}$, is known. For displacement boundary conditions, $\det \bar{\mathbf{F}}$ is of course known since it is prescribed. On the other hand, for traction and mixed boundary conditions, such as the one considered in this subsection, $\det \bar{\mathbf{F}}$ is not known a priori and must be computed from the material response. In this connection, we remark that what we have denoted by “exact” porosity in Fig. 5 corresponds to the

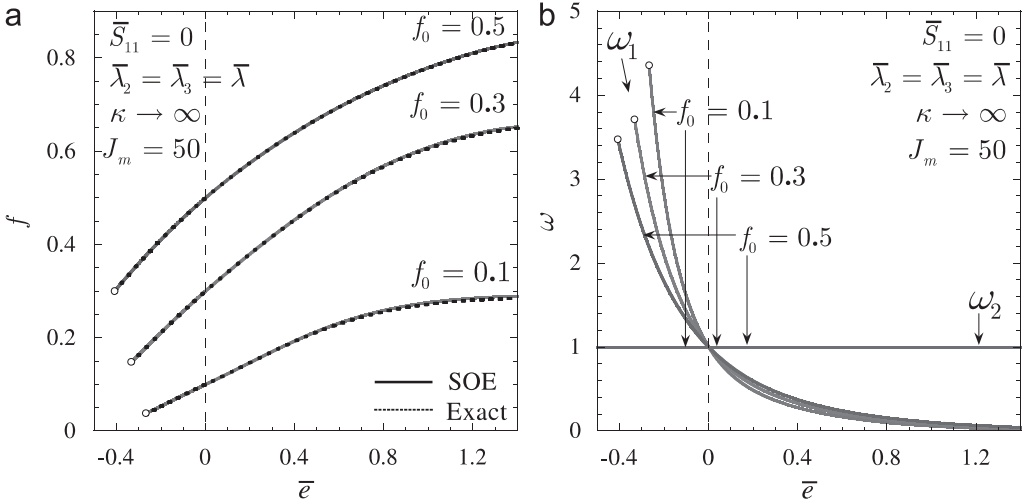


Fig. 5. Biaxial tension and compression ($\bar{\lambda}_2 = \bar{\lambda}_3 = \bar{\lambda}, \bar{S}_{11} = \partial \hat{\Phi}^I / \partial \bar{\lambda}_1 = 0$) of a porous elastomer with incompressible, Gent matrix phase with lock-up parameter $J_m = 50$ and various values of initial porosity f_0 . (a) The evolution of porosity f , as predicted by the second-order estimate (13), compared with the exact result. (b) The evolution of the aspect ratios ω_1 and ω_2 as predicted by the second-order estimate (13).

porosity generated by expression (31) in Part I evaluated at the $\det \bar{\mathbf{F}}$ predicted by the SOE (13). Having clarified this point we next note that Fig. 5(a) illustrates explicitly the fact already pointed out in Fig. 4(b) that the porosity increases for tensile loadings and decreases for compressive ones. The former mechanism induces geometric softening and the latter, stiffening. With regard to the evolution of the aspect ratios, we first notice from Fig. 5(b) that the average aspect ratio ω_2 remains identically equal to one throughout the entire loading process, as a result of the imposed macroscopic biaxial state of deformation (i.e., $\bar{\lambda}_2 = \bar{\lambda}_3$). On the other hand, the aspect ratio ω_1 is seen to decrease (increase) very significantly for tensile (compressive) loadings, entailing that the pores evolve on average into oblate (prolate) spheroids. In short, the pore ovalization resulting from the applied biaxial compression induces geometric softening on the overall stress–strain relation of the porous elastomer, while the development of “pancake” shapes for the pores resulting from tension induces geometric stiffening. Thus, in summary, the results illustrated in Fig. 5 make it plain that the evolution of the underlying microstructure is very different for biaxial compression than for tension. This is consistent with the fact that the porous elastomer loses strong ellipticity under biaxial compression and *not* under biaxial tension.

In order to gain further insight on the results shown in Figs. 4 and 5, Fig. 6 provides results for the normal ($\mathcal{L}_{1111}, \mathcal{L}_{2222}, \mathcal{L}_{3333}$) and shear ($\mathcal{L}_{1212}, \mathcal{L}_{1313}, \mathcal{L}_{2323}$) components of the normalized effective incremental modulus $\widehat{\mathcal{L}} = \mu^{-1} \partial^2 \widehat{W}^I / \partial \bar{\mathbf{F}}^2$ of a porous elastomer with Gent matrix phase ($J_m = 50$) and initial porosity of 30% under biaxial loading ($\bar{\lambda}_2 = \bar{\lambda}_3 = \bar{\lambda}, \bar{S}_{11} = \partial \hat{\Phi}^I / \partial \bar{\lambda}_1 = 0$). Part (a) shows results for biaxial compression ($\bar{\lambda} \leq 1$), and part (b), for biaxial tension ($\bar{\lambda} \geq 1$). Fig. 6(a) shows that—in agreement with the stress–strain results shown in Fig. 4(a)—the normal components $\widehat{\mathcal{L}}_{2222} = \widehat{\mathcal{L}}_{3333}$ increase monotonically with the applied compressive strain. Note also that the normal component $\widehat{\mathcal{L}}_{1111}$ increases monotonically as well. In contrast, the effective shear moduli

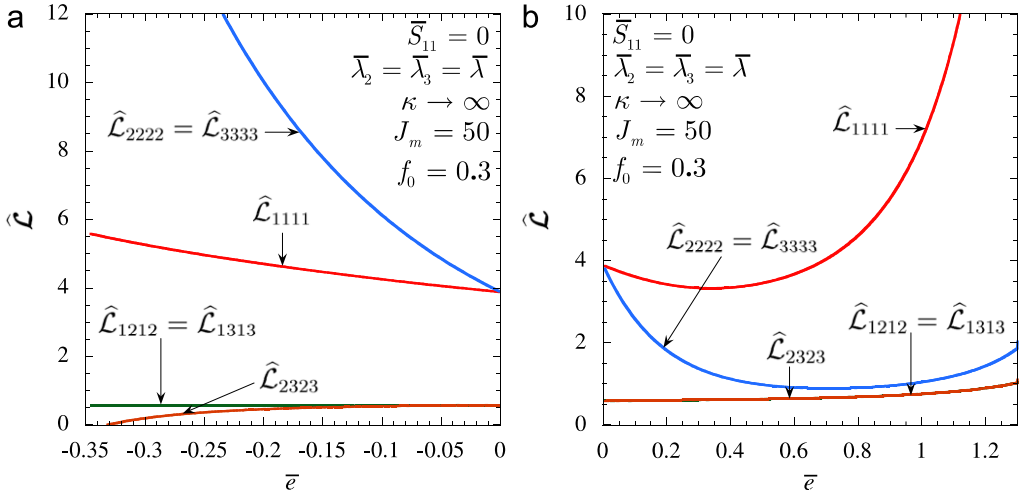


Fig. 6. Effective response, as predicted by the second-order estimate (13), of a porous elastomer with incompressible matrix phase subjected to biaxial tension and compression ($\bar{\lambda}_2 = \bar{\lambda}_3 = \bar{\lambda}$, $\bar{S}_{11} = \partial \hat{\Phi}^I / \partial \bar{\lambda}_1 = 0$). The results correspond to a material with Gent matrix phase ($J_m = 50$) and initial porosity of $f_0 = 30\%$ and are shown as a function of the logarithmic strain $\bar{e} = \ln \bar{\lambda}$. The normal and shear principal components of the effective incremental modulus $\hat{\mathcal{L}}$ for (a) biaxial compression ($\bar{\lambda} \leq 1$) and (b) biaxial tension ($\bar{\lambda} \geq 1$).

$\hat{\mathcal{L}}_{1212}$, $\hat{\mathcal{L}}_{1313}$, $\hat{\mathcal{L}}_{2323}$ are seen to decrease with increasing biaxial compression, especially $\hat{\mathcal{L}}_{2323}$ which vanishes at some critical finite stretch $\bar{\lambda}_{\text{crit}}$. This stretch corresponds precisely to the point at which the material loses strong ellipticity. In this connection, similar to the hydrostatic loading case, it should be noted that the combination $\hat{\mathcal{L}}_{2222}\hat{\mathcal{L}}_{3333} + \hat{\mathcal{L}}_{2323}^2 - (\hat{\mathcal{L}}_{2323} + \hat{\mathcal{L}}_{3232})^2 + 2\hat{\mathcal{L}}_{2323}\sqrt{\hat{\mathcal{L}}_{2222}\hat{\mathcal{L}}_{3333}}$ does also vanish at $\bar{\lambda}_{\text{crit}}$. Making contact with Appendix A of Part I, this means that conditions (33)₃ and (34)₃ in Part I cease to hold true. This implies that the porous elastomer may develop localized deformations in bands with normals $\mathbf{N} \in \text{Span}\{\mathbf{u}_2, \mathbf{u}_3\}$, where \mathbf{u}_2 and \mathbf{u}_3 denote the unit vectors defining the macroscopic Lagrangian principal axes associated with the principal stretches $\bar{\lambda}_2$ and $\bar{\lambda}_3$, respectively. Moreover, the vector \mathbf{m} associated with a given \mathbf{N} is such that $\mathbf{m} \perp \mathbf{N}$, so that the deformation localizes in shear within the bands. In other words, when subjected to biaxial compression, the porous elastomer may become infinitesimally soft under incremental shear deformations in planes with normals defined by the Lagrangian principal axes associated with the smallest principal stretches (which correspond to the largest compressive strains). As for the hydrostatic loading case, it should be emphasized that this behavior is rather subtle. Indeed, Fig. 5(a) shows that, under biaxial compression, the porous elastomer *stiffens* in the “direction” of the applied loading (i.e., $\hat{\mathcal{L}}_{2222} = \hat{\mathcal{L}}_{3333}$ increase with the applied stretch). However, its incremental shear response (in the \mathbf{u}_2 – \mathbf{u}_3 plane) *softens* to the point that the material loses strong ellipticity at some finite critical stretch $\bar{\lambda}_{\text{crit}}$ (at which $\hat{\mathcal{L}}_{2323} = \hat{\mathcal{L}}_{3232} = \hat{\mathcal{L}}_{2222}\hat{\mathcal{L}}_{3333} + \hat{\mathcal{L}}_{2323}^2 - (\hat{\mathcal{L}}_{2323} + \hat{\mathcal{L}}_{3232})^2 + 2\hat{\mathcal{L}}_{2323}\sqrt{\hat{\mathcal{L}}_{2222}\hat{\mathcal{L}}_{3333}} = 0$). Turning now to Fig. 6(b), it is observed that—in accord with the stress–strain results shown in Fig. 4(a)—the incremental normal moduli

$\widehat{\mathcal{L}}_{2222} = \widehat{\mathcal{L}}_{3333}$ initially decrease and then increase, as a function of the applied biaxial strain. On the other hand, the effective incremental shear moduli $\widehat{\mathcal{L}}_{1212}$, $\widehat{\mathcal{L}}_{1313}$, $\widehat{\mathcal{L}}_{2323}$ increase monotonically with the applied tensile strain, improving the stability of the porous elastomer. Even though the results illustrated in Fig. 6 correspond to $f_0 = 0.3$, they are representative of results for porous elastomers with any value of initial porosity f_0 . A more detailed investigation of the effect of f_0 on the effective incremental behavior and stability of porous elastomers subjected to biaxial loading will be addressed in the context of the next figure. As a final remark, it is appropriate to emphasize that the DPB model (11) (with Neo-Hookean matrix phase) can be shown to remain strongly elliptic for all biaxial tension/compression loading. This implies that the corresponding DPB estimate with Gent matrix phase (9) remains strongly elliptic for all biaxial tension/compression loading as well. This is easy to check by realizing that a Gent material (2) is stiffer than a Neo-Hookean material (3) for all modes of deformation.

Fig. 7 presents plots associated with the results shown in Fig. 3 for (a) the critical stretch, $\bar{\lambda}_{\text{crit}}$, and (b) the normalized critical stress, $\bar{S}_{\text{crit}}/\mu$, at which the SOE (13) loses strong ellipticity under biaxial compression as a function of the initial porosity f_0 . Fig. 7(a) illustrates that the stability of the porous material improves in strain space with increasing initial porosity, in accord with the results found for hydrostatic compression (see Fig. 3(a)). Notice, however, that the stretches $\bar{\lambda}_{\text{crit}}$ in Fig. 7(a) are significantly smaller than those in Fig. 3(a). In particular, it is observed that $\bar{\lambda}_{\text{crit}} \rightarrow \bar{\lambda}_{\text{crit}}^0$ with $\bar{\lambda}_{\text{crit}}^0 \approx 0.78$ as $f_0 \rightarrow 0$ for biaxial compression, whereas, for hydrostatic compression, $\bar{\lambda}_{\text{crit}} \rightarrow 1$ as $f_0 \rightarrow 0$. This implies that for biaxial compression $\bar{\lambda}_{\text{crit}}$ has a discontinuity at $f_0 = 0$, since for this type of loading $\bar{\lambda}_{\text{crit}} = 0$ at $f_0 = 0$ (due to the fact that the matrix phase is strongly elliptic for all isochoric deformations). Physically, this result suggests that the addition of even a small proportion of pores can have a dramatic effect on the overall stability of porous elastomers with incompressible, strongly elliptic matrix phases under certain type of finite deformations. In contrast to the results found

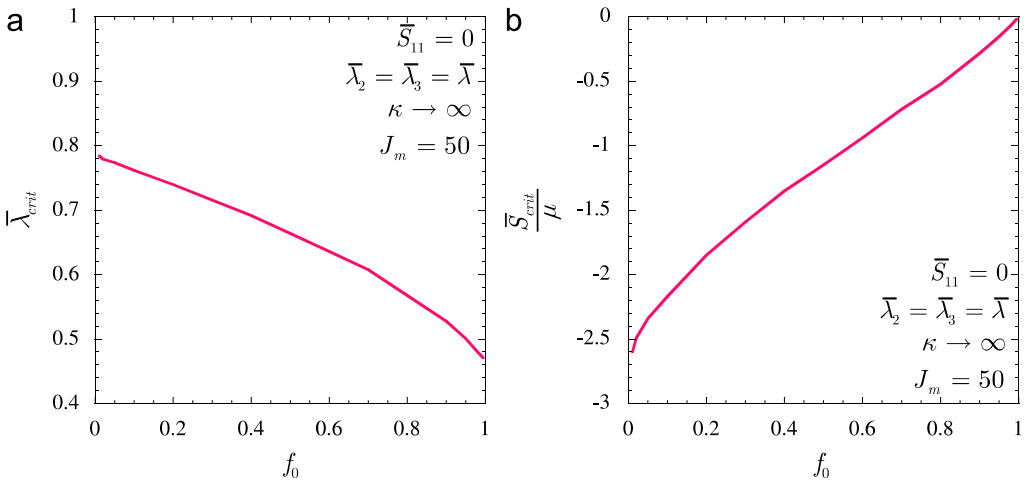


Fig. 7. Biaxial tension and compression ($\bar{\lambda}_2 = \bar{\lambda}_3 = \bar{\lambda}$, $\bar{S}_{11} = \partial\widehat{\Phi}^I/\partial\bar{\lambda}_1 = 0$) of a porous elastomer with incompressible, Gent matrix phase ($J_m = 50$) with various values of initial porosity f_0 . (a) The critical stretch $\bar{\lambda}_{\text{crit}}$ at which the second-order estimate (13) loses strong ellipticity as a function of initial porosity f_0 . (b) The corresponding critical stress $\bar{S}_{\text{crit}}/\mu$.

for hydrostatic compression, Fig. 7(b) shows that, in stress space, the porous elastomer becomes more unstable with increasing initial porosity throughout the entire physical domain $0 < f_0 < 1$. That is, $|\bar{S}_{crit}|$ decreases *monotonically* with increasing f_0 .

3.1.3. Uniaxial tension/compression

Fig. 8 shows the SOE predictions for the effective response of a porous elastomer with incompressible Gent matrix phase under uniaxial loading ($\bar{\lambda}_1 = \bar{\lambda}$, $\bar{S}_{22} = \partial\hat{\Phi}^I/\partial\bar{\lambda}_2 = \bar{S}_{33} = \partial\hat{\Phi}^I/\partial\bar{\lambda}_3 = 0$). Results are depicted for a matrix lock-up parameter of $J_m = 50$ and initial porosities of $f_0 = 0\%$, 10%, 30% and 50% as a function of the logarithmic strain $\bar{e} = \ln \bar{\lambda}$. Part (a) shows the normalized macroscopic “uniaxial” stress $\bar{S}_{uni}/\mu = \mu^{-1}\partial\hat{\Phi}^I/\partial\bar{\lambda}_1$, and part (b), the associated “lateral” strain $\bar{e}_{lat} = \ln \bar{\lambda}_2 = \ln \bar{\lambda}_3$. A glance at Fig. 8 suffices to remark its many similarities with Fig. 4 (for biaxial loading). Indeed, Fig. 8 shows that the effective stress–strain behavior of the porous elastomer is softer for higher values of the initial porosity f_0 and exhibits a very substantial stiffening for tension as well as compression. Additionally, the volume of the porous elastomer increases under uniaxial tension and decreases under uniaxial compression. That is, in the present context, $\ln(\det \bar{\mathbf{F}}) = 2\bar{e}_{lat} + \bar{e} > 0$ for $\bar{e} > 0$ and $2\bar{e}_{lat} + \bar{e} < 0$ for $\bar{e} < 0$. There are, however, two major differences worth of notice. First, we remark that while for biaxial tension (compression) the underlying pores evolve into oblate (prolate) spheroids, the opposite is true for uniaxial tension (compression). This has an important effect on the overall behavior and, especially, on the stability of the porous elastomer. In this connection, we note that, as opposed to biaxial compression, no loss of strong ellipticity takes place under uniaxial compression. In fact, the SOE predicts that for uniaxial compression the porosity will vanish at some finite stretch (denoted with the symbol “ \diamond ” in the plots) before any macroscopic instabilities take place.

For completeness, Fig. 9 illustrates the evolution of the relevant microstructural variables associated with the results shown in Fig. 8. Part (a) shows the evolution of the

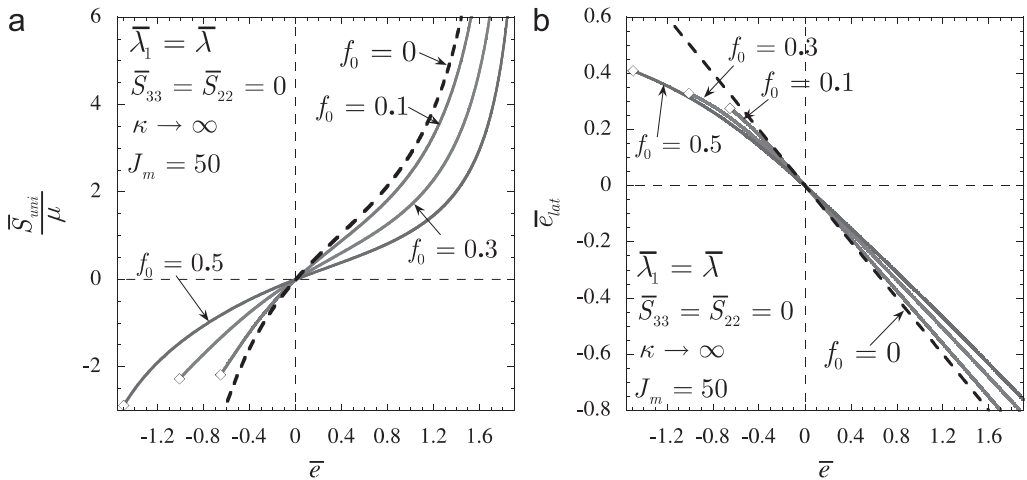


Fig. 8. Effective response, as predicted by the second-order estimate (13), of a porous rubber subjected to uniaxial tension and compression ($\bar{\lambda}_1 = \bar{\lambda}$, $\bar{S}_{22} = \partial\hat{\Phi}^I/\partial\bar{\lambda}_2 = \bar{S}_{33} = \partial\hat{\Phi}^I/\partial\bar{\lambda}_3 = 0$), as a function of the logarithmic strain $\bar{e} = \ln \bar{\lambda}$. The results correspond to a material with incompressible, Gent matrix phase with $J_m = 50$ and various values of initial porosity f_0 . (a) The normalized macroscopic stress $\bar{S}_{uni}/\mu = \mu^{-1}\partial\hat{\Phi}^I/\partial\bar{\lambda}_1$. (b) The lateral strain $\bar{e}_{lat} = \ln \bar{\lambda}_2 = \ln \bar{\lambda}_3$.

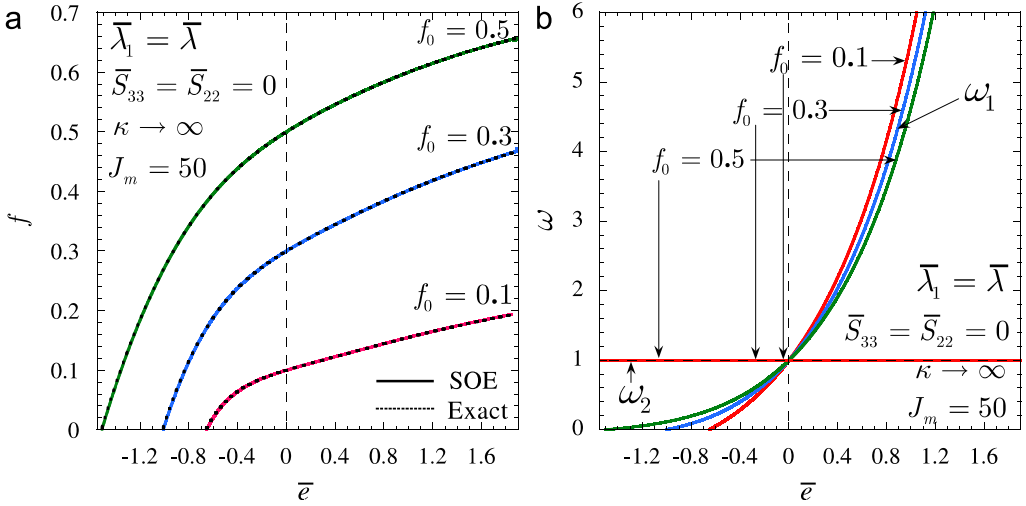


Fig. 9. Uniaxial tension and compression ($\bar{\lambda}_1 = \bar{\lambda}, \bar{S}_{22} = \partial\hat{\Phi}^I/\partial\bar{\lambda}_2 = \bar{S}_{33} = \partial\hat{\Phi}^I/\partial\bar{\lambda}_3 = 0$) of a porous elastomer with incompressible, Gent matrix phase with $J_m = 50$ and various values of initial porosity f_0 . (a) The evolution of porosity f , as predicted by the second-order estimate (13), compared with the exact result. (b) The evolution of the aspect ratios ω_1 and ω_2 as predicted by second-order estimate (13).

porosity f and part (b), the evolution of the aspect ratios ω_1 and ω_2 , as a function of the logarithmic strain $\bar{\epsilon} = \ln \bar{\lambda}$. First, note that the porosity f , as predicted by the SOE (13), is in excellent agreement with the “exact” result (as computed from expression (31) in Part I evaluated at the $\det \bar{\mathbf{F}}$ predicted by (13)). Note further that the aspect ratio ω_2 is identically equal to one throughout the entire loading process, as a consequence of the resulting macroscopic uniaxial state of deformation (i.e., $\bar{\lambda}_3 = \bar{\lambda}_2$ since $\bar{S}_{33} = \bar{S}_{22}$). On the other hand, $\omega_1 > (<)1$ for $\bar{\epsilon} > (<)0$, so that the initially spherical pores deform on average into prolate (oblate) spheroids under uniaxial tension (compression), corroborating the comments in the previous paragraph. In summary, the above-presented results for uniaxial loading induce similar geometric stiffening/softening effects to those found for biaxial loading. Namely, under uniaxial tension, the increase of porosity induces geometric softening and the pore ovalization, stiffening. Conversely, under uniaxial compression, the decrease of porosity induces geometric stiffening and the development of “pancake” shapes for the pores, softening.

3.1.4. Macroscopic failure surfaces

Fig. 10 illustrates the macroscopic failure surfaces, as determined by the loss of strong ellipticity of the SOE (13) (denoted by LOE in the plots). Results are given for a porous elastomer with incompressible Neo-Hookean matrix phase and initial porosities of $f_0 = 10\%$, 30% , and 50% . Part (a) shows failure surfaces for applied axisymmetric deformations ($\bar{\epsilon}_3 = \bar{\epsilon}_2$) in strain space, and part (b), for applied axisymmetric stresses ($\bar{S}_{33} = \bar{S}_{22}$) in stress space. For completeness, the boundary at which the porosity vanishes has also been included (dotted lines) in Fig. 10. Note that once the pore-closure boundary is reached, no further compressive (with $\bar{J} < 1$) deformation is possible.

Before proceeding with the bulk of the discussion, it is helpful to identify in Fig. 10 the loading paths considered in the three previous subsections. Thus, we note that the line

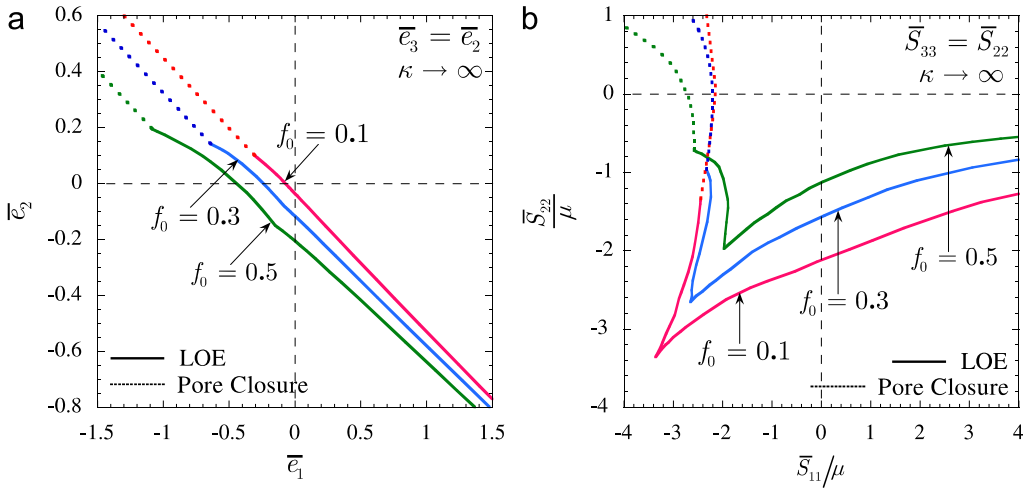


Fig. 10. Macroscopic onset-of-failure surface, as determined by the loss of strong ellipticity of the second-order estimate (13), for a porous elastomer with incompressible, Neo-Hookean matrix phase and various values of initial porosity. Part (a) illustrates the results for applied axisymmetric deformations ($\bar{e}_3 = \bar{e}_2$) in the \bar{e}_1 – \bar{e}_2 plane in strain space. Part (b) shows corresponding results for applied axisymmetric stresses ($\bar{S}_{33} = \bar{S}_{22}$) in the \bar{S}_{11} – \bar{S}_{22} plane in dimensionless stress space.

$\bar{e}_2 = \bar{e}_1$ in Fig. 10(a), as well as the line $\bar{S}_{22} = \bar{S}_{11}$ in Fig. 10(b), correspond precisely to hydrostatic loading, which was considered in detail in Figs. 1 and 3. Moreover, the lines $\bar{S}_{11} = 0$ and $\bar{S}_{22} = 0$ in Fig. 10(b) correspond to biaxial and uniaxial tension/compression, respectively. These loading paths were considered in detail in Figs. 4–7 and 8,9.

A key feature to remark from Fig. 10(a) is that the loci of points at which loss of strong ellipticity occurs satisfy the condition: $\ln(\det \bar{\mathbf{F}}) = \bar{e}_1 + \bar{e}_2 + \bar{e}_3 = \bar{e}_1 + 2\bar{e}_2 < 0$. Thus, according to the SOE (13), loss of strong ellipticity occurs necessarily under volume-reducing deformations. Or, in other words, the development of macroscopic instabilities may take place exclusively at “sufficiently” large *compressive* deformations. Another interesting point that deserves further comment is the trend followed by the onset of loss of strong ellipticity as a function of the initial porosity f_0 . In effect, the porous elastomer becomes more stable—in the sense that it loses strong ellipticity at larger strains—with increasing initial porosity. Recall that this behavior has already been observed in the context of hydrostatic and biaxial compression (see Figs. 3(a) and 7(a)). Fig. 10(a) illustrates, thus, that this counterintuitive trend applies more broadly to general axisymmetric loading conditions.

In parallel with Fig. 10(a), Fig. 10(b) shows that a necessary condition for loss of strong ellipticity to occur is the existence of a *compressive* component in the state of stress. Fig. 10(b) also illustrates that the porous elastomer becomes more unstable—in the sense that it loses strong ellipticity at smaller stresses—with increasing initial porosity f_0 . This trend is in contrast to that one observed in strain space. The explanation for such disparity follows that one given in the context of Fig. 3 (for hydrostatic compression). That is, given the drastically softer stress–strain relations of the porous elastomer for larger values of initial porosity, the strains required to reach the critical stresses happen to be larger for larger initial porosities.

Fig. 11 provides analogous results to those shown in Fig. 10 for a porous elastomer with an initial porosity of $f_0 = 30\%$ and Neo-Hookean matrix phase with compressibility ratios

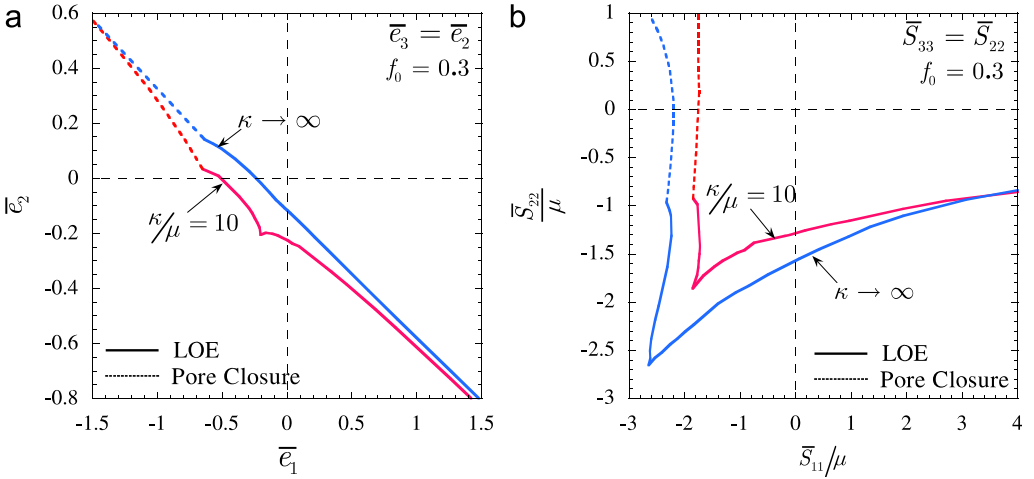


Fig. 11. Macroscopic onset-of-failure surface, as determined by the loss of strong ellipticity of the second-order estimates (12) and (13), for a porous elastomer with Neo-Hookean matrix phase and two values of compressibility ratio of the matrix phase. Part (a) illustrates the results for applied axisymmetric deformations ($\bar{e}_3 = \bar{e}_2$) in the \bar{e}_1 – \bar{e}_2 plane in strain space. Part (b) shows corresponding results for applied axisymmetric stresses ($\bar{S}_{33} = \bar{S}_{22}$) in the \bar{S}_{11} – \bar{S}_{22} plane in dimensionless stress space.

$\kappa/\mu = 10$ and $\kappa \rightarrow \infty$. Part (a) shows the macroscopic failure surfaces for applied axisymmetric deformations ($\bar{e}_3 = \bar{e}_2$) in strain space, and part (b), for applied axisymmetric stresses ($\bar{S}_{33} = \bar{S}_{22}$) in stress space. The main observation that can be made from Fig. 11 is that the effect of compressibility of the matrix phase, as measured by the bulk modulus κ , on the overall stability of porous elastomers is opposite to that of the initial porosity f_0 . Namely, in strain space, the porous elastomer loses strong ellipticity at smaller strains for larger bulk modulus. On the other hand, in stress space, the porous elastomer loses strong ellipticity at larger stresses for larger bulk modulus. In this regard, we notice that by increasing the bulk modulus of the matrix phase we are effectively *constraining* the matrix material to deform isochorically. This results in an overall stiffening of the matrix phase, and therefore, also of the porous elastomer. In turn, the critical stresses at which the material loses strong ellipticity increase, while the corresponding critical strains decrease, with increasing κ .

Finally, it is appropriate to mention that the Neo-Hookean results shown in Figs. 10 and 11 are representative of results for Gent porous elastomers with any value of the material lock-up parameter J_m . Indeed, according to the SOE predictions, the lock-up parameter J_m has virtually no effect on the onset of loss of strong ellipticity. This is consistent with the fact that loss of strong ellipticity occurs mostly at compressive states of deformation, at which the effect of J_m is not “felt.”

3.2. Plane-strain loadings

3.2.1. Pure shear

In Fig. 12, SOE predictions are given for the pure shear loading ($\bar{\lambda}_1 = \bar{\lambda}$, $\bar{\lambda}_2 = \bar{\lambda}^{-1}$, $\bar{\lambda}_3 = 1$) of a porous elastomer with incompressible Gent matrix phases. Results are shown for an initial porosity of $f_0 = 10\%$ and matrix lock-up parameters of $J_m = 50$ and $J_m \rightarrow \infty$, as

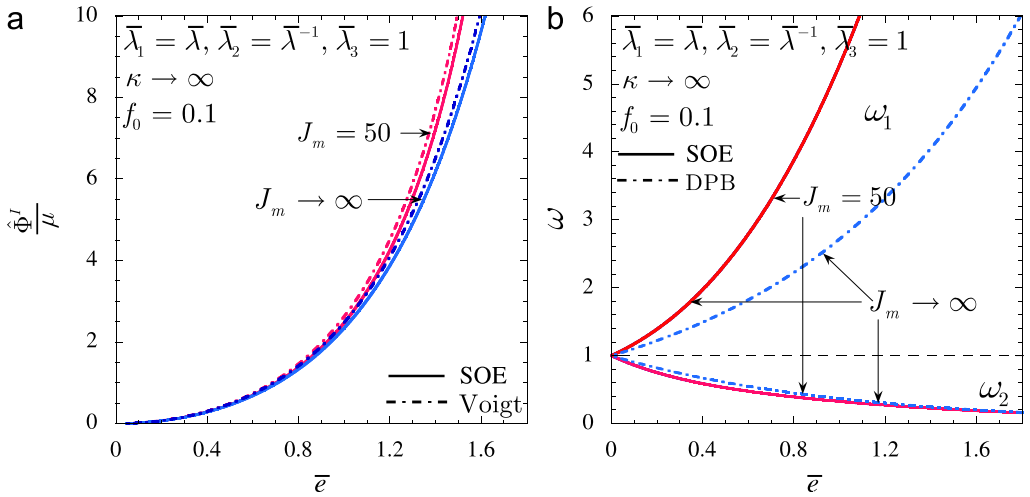


Fig. 12. Effective response of a porous rubber with an incompressible, Gent matrix phase subjected to pure shear ($\bar{\lambda}_1 = \bar{\lambda}, \bar{\lambda}_2 = \bar{\lambda}^{-1}, \bar{\lambda}_3 = 1$), as a function of the logarithmic strain $\bar{\epsilon} = \ln \bar{\lambda}$. (a) The normalized effective stored-energy function $\hat{\Phi}'/\mu$ as predicted by the second-order estimate (13) and the Voigt bound (6). (b) The evolution of the aspect ratios of the underlying pores, ω_1 and ω_2 . Part (b) also includes the aspect ratios as predicted by the DPB model (11).

a function of the logarithmic strain $\bar{\epsilon} = \ln \bar{\lambda}$. First, we note from Fig. 12(a) that the SOE predictions satisfy the rigorous Voigt upper bound (6). Recall that this bound is only helpful for isochoric deformations (i.e., deformations with $\det \bar{\mathbf{F}} = 1$), like the one considered in this subsection, since it becomes unbounded otherwise. Recall as well that the DPB model (11) coincides exactly with the Voigt bound (6) in this case. In connection with the evolution of the microstructure, it should be remarked that the porosity does not evolve under pure shear deformations (i.e., $f = f_0$). On the other hand, as shown in Fig. 12(b), the aspect ratios, ω_1 and ω_2 , of the underlying pores do evolve substantially with increasing strain. In particular ω_1 increases while ω_2 decreases with increasing $\bar{\epsilon}$. It is also interesting to observe that the evolution of the aspect ratios appears to be practically insensitive to the value of the matrix lock-up parameter J_m . For comparison purposes, we have included in Fig. 12(b) the evolution of the aspect ratios ω_1 and ω_2 as predicted by the DPB model (11) for the case of $J_m \rightarrow \infty$. In this regard, it is noticed that the DPB result for ω_2 is very similar to the corresponding SOE prediction. On the other hand, the aspect ratio ω_1 , as computed from the DPB model, is largely below the SOE result. This has the direct implication that, in the direction of the applied tensile stretch $\bar{\lambda}_1 = \bar{\lambda}$, the DPB model should exhibit a weaker geometric stiffening—due to pore ovalization—than the SOE. By the same token, it should also exhibit a stronger geometric stiffening in the direction of the applied compressive stretch $\bar{\lambda}_2 = \bar{\lambda}^{-1}$. As a final point, it should be remarked that no loss of ellipticity is observed for any level of pure shear deformation from any of the models.

Fig. 13 provides corresponding results for the normalized stress components (a) \bar{S}_{11}/μ and (b) \bar{S}_{22}/μ as a function of the logarithmic strain $\bar{\epsilon} = \ln \bar{\lambda}$. SOE predictions are given for values of the matrix lock-up parameter of $J_m = 50$ and $J_m \rightarrow \infty$. DPB predictions are given only for $J_m \rightarrow \infty$. Fig. 13 clearly shows that the material parameter J_m has a strong effect on the behavior of the porous elastomer. This is not surprising since the response of

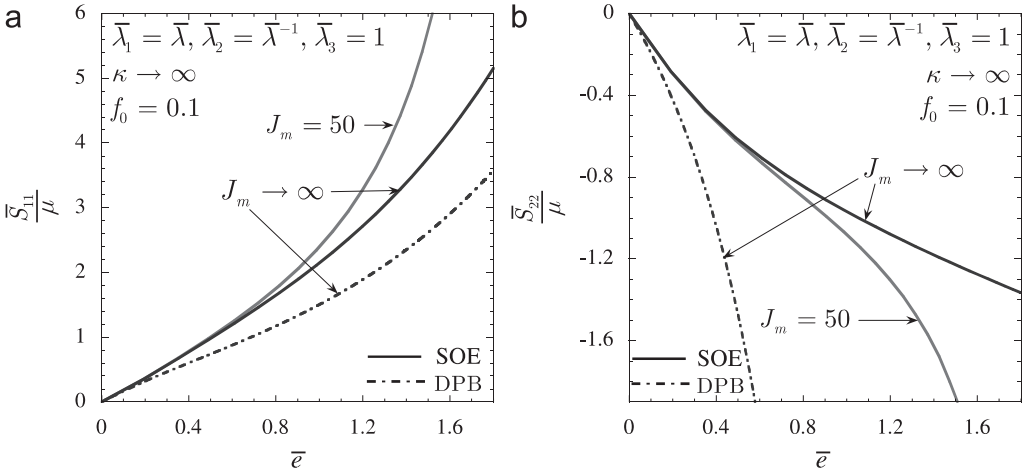


Fig. 13. Effective response of a porous rubber with an incompressible Gent matrix phase subjected to pure shear ($\bar{\lambda}_1 = \bar{\lambda}, \bar{\lambda}_2 = \bar{\lambda}^{-1}, \bar{\lambda}_3 = 1$) as a function of the logarithmic strain $\bar{e} = \ln \bar{\lambda}$. (a) The normalized macroscopic stress \bar{S}_{11}/μ . (b) The normalized macroscopic stress \bar{S}_{22}/μ .

the matrix phase is itself also highly dependent on J_m . Furthermore, we notice that both stress components exhibit substantial stiffening with the applied stretch. In this regard, we remark that (for $J_m \rightarrow \infty$) the SOE prediction for the component \bar{S}_{11}/μ is much stiffer than the corresponding DPB estimate, while the opposite is true for the component \bar{S}_{22}/μ . This behavior is entirely consistent with the observations made in Fig. 12(b), where it was concluded that the pore ovalization predicted by the DPB model induces a stronger geometric softening (stiffening) in the direction of the tensile (compressive) stretch $\bar{\lambda}_1 = \bar{\lambda}$ ($\bar{\lambda}_2 = \bar{\lambda}^{-1}$) than the one predicted by the SOE.

3.2.2. *In-plane uniaxial tension/compression*

Fig. 14 provides results for the overall response of a porous elastomer with incompressible Neo-Hookean matrix phase under plane-strain *tension* ($\bar{\lambda}_1 = \bar{\lambda} \geq 1, \bar{\lambda}_3 = 1, \bar{S}_{22} = \partial \hat{\Phi}^I / \partial \bar{\lambda}_2 = 0$). Results are shown for the second-order (13) and the DPB (11) estimates, and finite element (FEM) calculations (from Danielsson et al., 2004) for initial porosities of 5%, 15%, and 25% as a function of the logarithmic strain $\bar{e} = \ln(\bar{\lambda})$. Part (a) shows the normalized macroscopic Cauchy stress $\bar{T}/\mu = \mu^{-1}(1/\bar{\lambda}_2)\partial \hat{\Phi}^I / \partial \bar{\lambda}_1$, and part (b), the associated lateral strain $\bar{e}_{\text{lat}} = \ln \bar{\lambda}_2$.

Before proceeding with the discussion of Fig. 14, it is necessary to make the following clarifications. First, the FEM results illustrated in Fig. 14 correspond to the effective response of a multi-void cell model consisting of a random assembly of cubes that are either solid or contain an initially spherical void. (For further details on the cell model see Danielsson et al., 2004.) The microstructure of this multi-void cell model is thus *monodisperse*, in contrast to the polydisperse microgeometry assumed by the SOE and the DPB models. Nevertheless, for the small and moderate values of porosity considered in the results shown in Fig. 14, the dispersion in the size of pores is not expected to be of critical importance on the overall response of the material. Second, it should be mentioned that the Cauchy stress $\bar{T}/\mu = \mu^{-1}(1/\bar{\lambda}_2)\partial \hat{\Phi}^I / \partial \bar{\lambda}_1$, as opposed to the first Piola–Kirchhoff stress $\bar{S}/\mu = \mu^{-1}\partial \hat{\Phi}^I / \partial \bar{\lambda}_1$, is shown in Fig. 14(a) for two reasons: the FEM results were originally

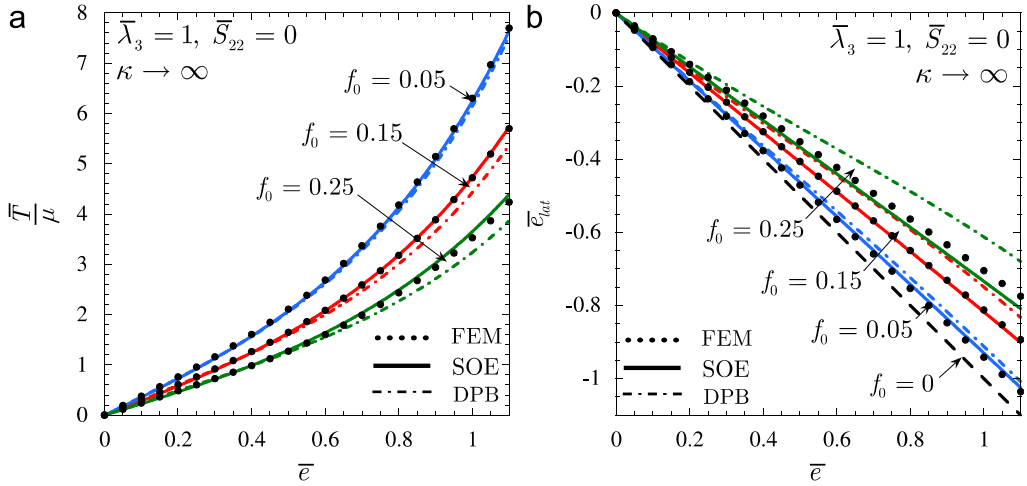


Fig. 14. Effective response of a porous rubber subjected to plane-strain tension ($\bar{\lambda}_1 = \bar{\lambda} \geq 1, \bar{\lambda}_3 = 1, \bar{S}_{22} = \partial \hat{\Phi}^f / \partial \bar{\lambda}_2 = 0$), as a function of the logarithmic strain $\bar{\epsilon} = \ln \bar{\lambda}$. Comparisons between the SOE predictions, the Danielsson–Parks–Boyce model (DPB), and FEM results for a material with incompressible, Neo-Hookean matrix phase and various values of initial porosity f_0 . (a) The normalized macroscopic Cauchy stress $\bar{T}/\mu = \mu^{-1}(1/\bar{\lambda}_2)\partial \hat{\Phi}^f / \partial \bar{\lambda}_1$. (b) The lateral strain $\bar{\epsilon}_{\text{lat}} = \ln \bar{\lambda}_2$.

provided for this variable in Danielsson et al. (2004), and it brings out more clearly the differences between the two compared estimates with the FEM results.

Fig. 14 shows that the SOE predictions are in excellent agreement with the FEM calculations. Interestingly, the DPB model delivers estimates that are in very good agreement with the numerical calculations for the case of $f_0 = 5\%$, but, for larger initial porosities, the agreement between the DPB predictions and the FEM (and hence the SOE) results deteriorates noticeably, especially for larger initial porosities f_0 . It is also noted that the stress–strain curves in Fig. 14(a) exhibit a pronounced stiffening with increasing strain. With regard to Fig. 14(b), we notice that all three estimates indicate that the volume of the porous elastomer increases when the material is subjected to plane-strain tension, that is, $\bar{\epsilon} + \bar{\epsilon}_{\text{lat}} > 0$. (The line $\bar{\epsilon} + \bar{\epsilon}_{\text{lat}} = 0$, which corresponds to $f_0 = 0$, has been included in Fig. 14(b) for reference purposes.) Again, since the elastomeric matrix phase is incompressible, this has the direct implication that the porosity increases with the applied deformation.

Fig. 15 provides analogous results to those shown in Fig. 14 for plane-strain compression ($\bar{\lambda}_1 = \bar{\lambda} \leq 1, \bar{\lambda}_3 = 1, \bar{S}_{22} = \partial \hat{\Phi}^f / \partial \bar{\lambda}_2 = 0$). Unfortunately, no FEM results were reported in Danielsson et al. (2004) for this loading, and hence, attention is confined to the SOE and the DPB predictions. Fig. 15(a) shows that the predictions from the DPB model are much stiffer than the corresponding SOE results. This disparity, as it will be explained in more detail in the discussion of Fig. 16, is due to different predictions of the evolution of microstructure. Next, note that both models predict that the porous elastomer remains stable for all applied plane-strain compression. However, while the SOE predicts that the porosity will vanish at some finite compressive strain (indicated with the symbol “ \diamond ” in the plots), the DPB model predicts that zero porosity is never reached under plane-strain compression. We conclude by remarking from Fig. 15(b) that the volume of the porous

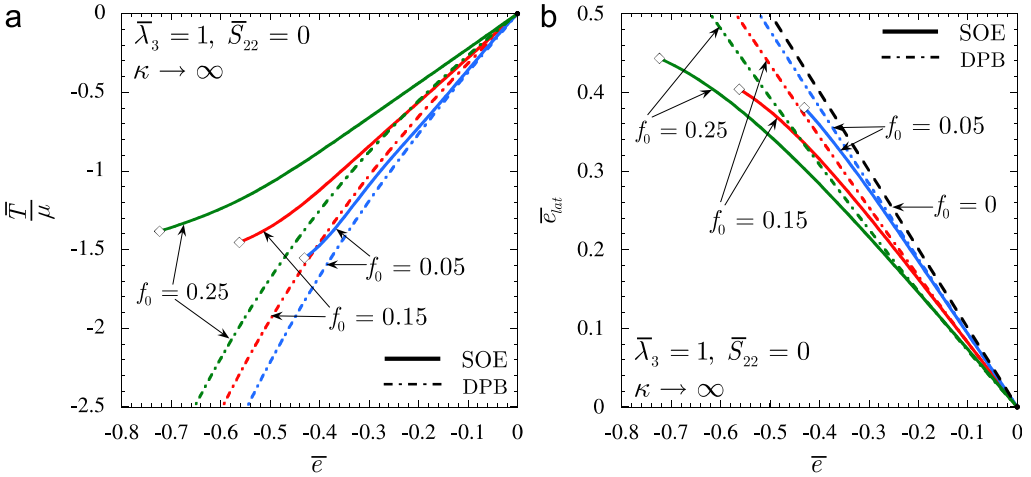


Fig. 15. Effective response of a porous rubber subjected to plane-strain compression ($\bar{\lambda}_1 = \bar{\lambda} \leq 1, \bar{\lambda}_3 = 1, \bar{S}_{22} = \partial \hat{\Phi}^I / \partial \bar{\lambda}_2 = 0$), as a function of the logarithmic strain $\bar{e} = \ln \bar{\lambda}$. Comparisons between the SOE and the Danielsson–Parks–Boyce (DPB) predictions for a material with incompressible, Neo-Hookean matrix phase and various values of initial porosity f_0 . (a) The normalized macroscopic Cauchy stress $\bar{T}/\mu = \mu^{-1}(1/\bar{\lambda}_2)\partial \hat{\Phi}^I / \partial \bar{\lambda}_1$. (b) The lateral strain $\bar{e}_{\text{lat}} = \ln \bar{\lambda}_2$.

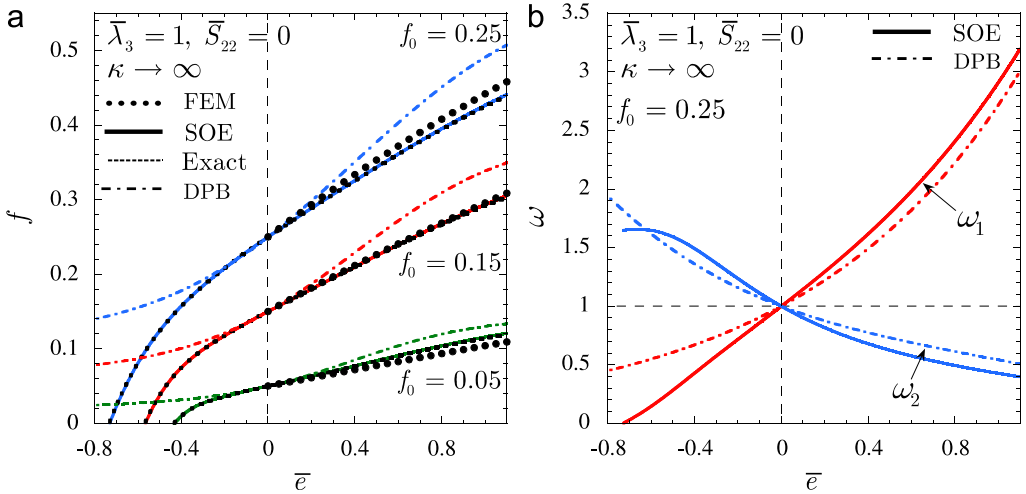


Fig. 16. Plane-strain tension and compression ($\bar{\lambda}_1 = \bar{\lambda}, \bar{\lambda}_3 = 1, \bar{S}_{22} = \partial \hat{\Phi}^I / \partial \bar{\lambda}_2 = 0$) of a porous elastomer with incompressible, Neo-Hookean matrix phase with various values of initial porosity f_0 . Comparisons between the SOE and the Danielsson–Parks–Boyce (DPB) predictions for (a) the evolution of porosity f , and (b) the evolution of the aspect ratios ω_1 and ω_2 .

elastomer decreases with the applied plane-strain compression, that is, $\bar{e} + \bar{e}_{\text{lat}} < 0$. (Similar to Fig. 14(b), the line $\bar{e} + \bar{e}_{\text{lat}} = 0$, denoting the response of the incompressible elastomeric matrix, has been included in Fig. 15(b) for reference purposes.)

Fig. 16 provides plots associated with the results shown in Fig. 14 and Fig. 15 for the effective behavior of a porous elastomer with incompressible Neo-Hookean matrix phase

under plane-strain loading (*tension* and *compression*). Part (a) shows the evolution of the porosity f for initial porosities of $f_0 = 5, 15,$ and 25% as a function of the applied strain $\bar{\epsilon} = \ln \bar{\lambda}$. Part (b) shows the evolution of the aspect ratios ω_1 and ω_2 for an initial porosity of $f_0 = 25\%$ as a function of the applied strain $\bar{\epsilon} = \ln \bar{\lambda}$. Fig. 16(a) shows that while the SOE predictions for the evolution of the porosity under plane-strain tension are in good agreement with the FEM calculations, the DPB predictions deviate significantly. Moreover, Fig. 16(a) illustrates explicitly the fact already revealed within the discussion of Fig. 14(b) and Fig. 15(b) that the porosity increases for plane-strain tension and decreases for plane-strain compression. In this regard, we note that the porosity predicted by the DPB model is always larger than the one predicted by the SOE (13), which entails that for plane-strain tension ($\bar{\epsilon} > 0$) the DPB model predicts a larger geometric softening due to changes in porosity than the SOE, and, by the same token, a weaker geometric stiffening for plane-strain compression ($\bar{\epsilon} < 0$). Furthermore, as already remarked in Fig. 15, it is seen that under plane-strain compression the DPB porosity does not vanish at a finite strain as the SOE predicts, but instead, reaches a horizontal asymptote. To conclude with Fig. 16(a), we remark that the evolution of the porosity f , as determined from the SOE (13), is in excellent agreement with the “exact” result, as computed from expression (31) in Part I (evaluated at the $\det \bar{\mathbf{F}}$ predicted by (13)). Turning now to Fig. 16(b), we notice that the aspect ratio ω_1 increases while ω_2 decreases for plane-strain tension. The opposite trend is observed for plane-strain compression. We also recognize that while the DPB predictions are similar to the SOE results for tension, they deviate significantly for compression. In this connection, note that the DPB prediction for ω_1 under plane-strain compression is largely above the corresponding SOE result, which is seen to vanish at some finite strain. In view of the fact that the decrease of ω_1 induces geometric softening in the present context, this strong disparity contributes to explain why the DPB predictions for the stress–strain relations in Fig. 15(a) are stiffer than the corresponding SOE results.

3.2.3. Macroscopic failure surfaces

Fig. 17 shows the macroscopic failure surfaces, as determined by the loss of strong ellipticity of the SOE (13), for a porous elastomer with incompressible, Neo-Hookean matrix phase and initial porosities of $f_0 = 10\%, 30\%$ and 50% under plane-strain loading ($\bar{\epsilon}_3 = 0$). Part (a) shows the results in strain space, and part (b), in stress space. For completeness, the boundary at which the porosity vanishes has also been included in Fig. 17.

Similar to Fig. 10(a) for axisymmetric loading, Fig. 17(a) shows that loss of strong ellipticity can only take place for volume-reducing deformations. More specifically, in the present context, the loci of points at which loss of strong ellipticity occurs satisfy the condition $\ln(\det \bar{\mathbf{F}}) = \bar{\epsilon}_1 + \bar{\epsilon}_2 + \bar{\epsilon}_3 = \bar{\epsilon}_1 + \bar{\epsilon}_2 < 0$. Also in accord with Fig. 10(a), Fig. 17(a) depicts that Neo-Hookean porous elastomers subjected to plane-strain loadings improve their stability in strain space with increasing initial porosity. As a final remark, it is interesting to note that the results shown in Fig. 10(a) are qualitatively similar to those previously found for porous elastomers with 2D random, isotropic microstructures (see Lopez-Pamies and Ponte Castañeda, 2004, Fig. 7). However, in quantitative terms, the 3D-microstructure material is more unstable (in strain space) than the 2D one, as loss of strong ellipticity occurs at smaller strains.

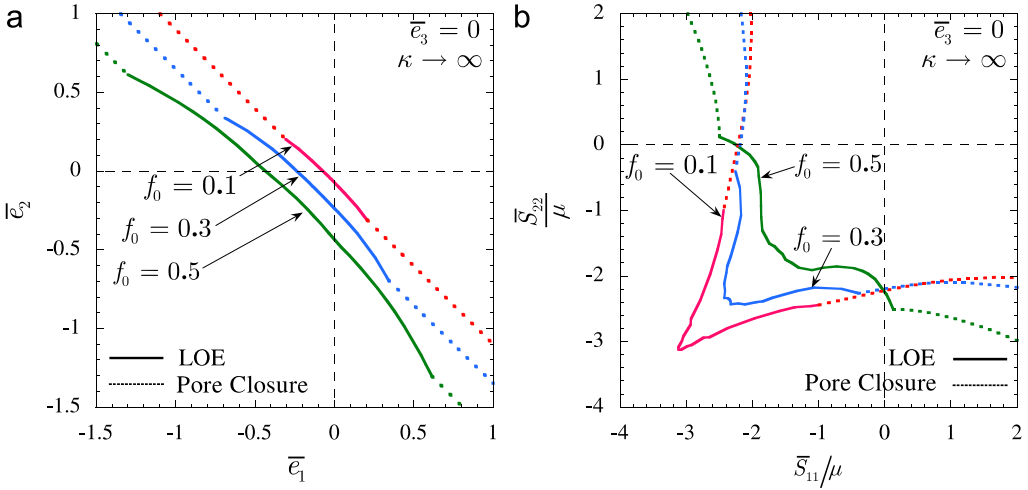


Fig. 17. Macroscopic onset-of-failure surface, as determined by the loss of strong ellipticity of the second-order estimate (13), for a porous elastomer with incompressible, Neo-Hookean matrix phase and various values of initial porosity under plane-strain loading ($\bar{e}_3 = 0$). (a) Failure surface in strain space. (b) The corresponding failure surface in dimensionless stress space.

Consistent with all previous results, Fig. 17(b) shows that a necessary condition for loss of strong ellipticity to occur is the existence of a *compressive* component in the state of stress. In fact, note that for $f_0 < 0.5$ both components of the stress must be compressive. In this regard, it is emphasized that the corresponding stress \bar{S}_{33} (not shown in the figure) is positive. (Recall that the results correspond to plane-strain conditions, i.e., $\bar{e}_3 = 0$.) This is in accord with the results shown in Fig. 13(b) for axisymmetric loading, where loss of strong ellipticity could occur at states with two components of stress being compressive (with the other component being tensile). Moreover, it is observed that in stress space the porous elastomer is more unstable for larger values of the initial porosity, in accord with preceding results. The reasons for this behavior parallel those given in the context of Fig. 10 (for axisymmetric loading conditions).

4. Concluding remarks

In this paper, use has been made of the homogenization-based constitutive model developed in Part I to generate comprehensive predictions for the stress–strain relation, the evolution of microstructure, and the onset of macroscopic instabilities in Gent porous elastomers under a wide range of loading conditions and values of initial porosity.

In accord with other elastomeric systems subjected to finite deformations (see, e.g., Lopez-Pamies and Ponte Castañeda, 2006b), the predictions generated in this work indicate that the evolution of the underlying microstructure has a very significant and subtle effect on the mechanical response of isotropic porous elastomers. In particular, it has been observed that the decrease of porosity—induced by macroscopic, volume-reducing loadings—produces *geometric stiffening* of the effective incremental response of the material in the “direction” of the applied loading. At the same time—and rather interestingly—the decrease of porosity does also lead to the *geometric softening* of the

effective incremental shear response of the material. Similarly, the change in shape of the underlying pores, as measured by their average aspect ratios, has also been identified as a geometric mechanism that can produce stiffening of the effective incremental response of the porous elastomer in some directions and softening in others.

An important consequence of the aforementioned softening mechanisms is that the “second-order” estimates for the effective behavior of porous elastomers can lose strong ellipticity, even in the case when the underlying matrix phase material is taken to be strongly elliptic. Thus, in this work, loss of strong ellipticity has been found to occur under sufficiently large macroscopic, *compressive* stresses and strains. In other words, according to the predictions, the onset of macroscopic instabilities—as determined by loss of strong ellipticity—for the class of porous elastomers under consideration in this work is driven by the applied *compressive loading*. In this connection, it is worth remarking that the recent model of Danielsson et al. (2004), which is based on a generalization of the earlier Voigt bound (Ogden, 1978) and Hashin (1985) estimate, is strongly elliptic for all deformations, and is thus unable to capture the expected development of instabilities under compressive loading.

Finally, the results generated in this paper have been shown to be in good agreement with exact and numerical results available from the literature for special loading conditions, and generally improve on existing models for more general loading conditions. In particular—as already stated—the new model proposed here predicts the development of macroscopic instabilities for loading conditions where such instabilities are expected to occur from numerical simulations (Triantafyllidis et al., 2006; Michel et al., 2007), as well as from physical evidence (Kinney et al., 2001; Gong and Kyriakides, 2005). This is in contrast with prior homogenization- and micromechanics-based models that fail to predict the development of such instabilities. Thus, although somewhat more difficult to implement than earlier homogenization estimates and micromechanics models, which make use of simpler trial fields and micromechanical hypotheses, the second-order method could prove to become a very useful tool in the development of accurate—but still computationally tractable—models for porous, as well as for other types of elastomeric composites.

Acknowledgments

This work was supported by NSF Grant DMS-0204617 and NSF/CNRS Grant OISE-02-31867.

References

- Danielsson, M., Parks, D.M., Boyce, M.C., 2004. Constitutive modeling of porous hyperelastic materials. *Mech. Mater.* 36, 347–358.
- Gent, A.N., 1996. A new constitutive relation for rubber. *Rubber Chem. Technol.* 69, 59–61.
- Geymonat, G., Müller, S., Triantafyllidis, N., 1993. Homogenization of nonlinearly elastic materials, microscopic bifurcation and macroscopic loss of rank-one convexity. *Arch. Ration. Mech. Anal.* 122, 231–290.
- Gong, L., Kyriakides, S., 2005. Compressive response of open-cell foams. Part II: initiation and evolution of crushing. *Int. J. Solids Struct.* 42, 1381–1399.
- Gurson, A.L., 1977. Continuum theory of ductile rupture by void nucleation and growth: part I—yield criteria and flow rules for porous ductile media. *J. Eng. Mater. Technol.* 99, 2–15.
- Hashin, Z., 1962. The elastic moduli of heterogeneous materials. *J. Appl. Mech.* 29, 143–150.

- Hashin, Z., 1985. Large isotropic elastic deformation of composites and porous media. *Int. J. Solids Struct.* 21, 711–720.
- Hou, H.-S., Abeyaratne, R., 1992. Cavitation in elastic and elastic–plastic solids. *J. Mech. Phys. Solids* 40, 571–592.
- Kinney, J.H., Marshall, G.W., Marshall, S.J., Haupt, D.L., 2001. Three-dimensional imaging of large compressive deformations in elastomeric foams. *J. Appl. Polym. Sci.* 80, 1746–1755.
- Lopez-Pamies, O., Ponte Castañeda, P., 2004. Second-order estimates for the macroscopic response and loss of ellipticity in porous rubbers at large deformations. *J. Elasticity* 76, 247–287.
- Lopez-Pamies, O., Ponte Castañeda, P., 2006a. On the overall behavior, microstructure evolution, and macroscopic stability in reinforced rubbers at large deformations: I—theory. *J. Mech. Phys. Solids* 54, 807–830.
- Lopez-Pamies, O., Ponte Castañeda, P., 2006b. On the overall behavior, microstructure evolution, and macroscopic stability in reinforced rubbers at large deformations. II—application to cylindrical fibers. *J. Mech. Phys. Solids* 54, 831–863.
- Lopez-Pamies, O., Ponte Castañeda, P., 2007. Homogenization-based constitutive models for porous elastomers and implications for macroscopic instabilities: I—analysis. *J. Mech. Phys. Solids*, in press, doi:10.1016/j.jmps.2007.01.007.
- Michel, J.-C., Lopez-Pamies, O., Ponte Castañeda, P., Triantafyllidis, N., 2007. Microscopic and macroscopic instabilities in finitely strained porous elastomers. *J. Mech. Phys. Solids*, in press, doi:10.1016/j.jmps.2006.11.006.
- Ogden, R., 1978. Extremum principles in non-linear elasticity and their application to composites—I theory. *Int. J. Solids Struct.* 14, 265–282.
- Triantafyllidis, N., Bardenhagen, S.G., 1996. The influence of scale size on the stability of periodic solids and the role of associated higher order gradient continuum models. *J. Mech. Phys. Solids* 44, 1891–1928.
- Triantafyllidis, N., Nestorvić, M.D., Schraad, M.W., 2006. Failure surfaces for finitely strained two-phase periodic solids under general in-plane loading. *J. Appl. Mech.* 73, 505–515.
- Wang, A.S.D., Ertepinar, A., 1972. Stability and vibrations of elastic thick-walled cylindrical and spherical shells subjected to pressure. *Int. J. Non-Linear Mech.* 7, 539–555.
- Wesolowski, Z., 1967. Stability of elastic thick-wall spherical shell loaded by external pressure. *Arch. Mech. Stosow.* 19, 3–23.